Title
Towards Understanding a Dynamic Cephalopod Protein Reflectin

Author
Naughton, Kyle Liam

Publication Date
2017

UNIVERSITY OF CALIFORNIA,
IRVINE

Towards Understanding a Dynamic Cephalopod Protein Reflectin

THESIS

submitted in partial satisfaction of the requirements
for the degree of

MASTER OF SCIENCE

in Physics

by

Kyle Liam Naughton

Thesis Committee:
Professor Alon A. Gorodetsky, Chair
Professor Zuzanna Siwy
Professor Jun Allard

2017

TABLE OF CONTENTS

LIST OF FIGURES iii
LIST OF TABLES x
AKNOWLEDGMENTS x
ABSTRACT OF THE THESIS xii
CHAPTER 1 Dynamic Materials Inspired by Cephalopods 1
1.1 Abstract 1
1.2 Introduction 1
1.3 Discussion 6
    1.3.1 Switchable Coloration 6
    1.3.2 Shape and Texture Modulation 20
1.4 Conclusions 26
1.5 References 30
CHAPTER 2 Self-Assembly of the Cephalopod Protein Reflectin 37
2.1 Abstract 37
2.2 Introduction 37
2.3 Experiment 40
    2.3.1 Dynamic Light Scattering of Reflectin 40
    2.3.2 Deuteron Exchange Mass Spectroscopy of Reflectin 41
    2.3.3 Small-angle X-Ray Scattering of Reflectin 44
    2.3.4 Scanning Electron Microscopy of Reflectin 51
    2.3.5 Grazing-incidence small-angle X-ray scattering of Reflectin 53
    2.3.6 Grazing-incidence wide-angle X-ray scattering of Reflectin 59
2.4 Results 62
2.5 Conclusion 65
2.6 References 66
CHAPTER 3 Summary and Future Work 78
3.1 Summary 78
3.2 Future Work 78
3.3 References 81

LIST OF FIGURES

Figure 1.1. **Illustrations of camouflage through history.** A) A painting by Giuseppe Arcimboldo of Vertumnus, the Roman mythological god of seasons, who is able to alter his form at will. B) A painting by Paulus Moreelse, in which Vertumnus has changed form into an old woman to woo Pomona. C) A medieval woodcut by Hans Weiditz of a human who has transformed into a wolf and is attacking two men. Part A) painting Public domain was reproduced via Wikimedia Commons. Part B) painting Public domain was reproduced via Wikimedia Commons. Part C) woodcut Public domain was reproduced via Wikimedia Commons. 2

Figure 1.2. Optical Images of cephalopods changing appearance to blend into their environment A) A camouflaged octopus positioned on a rock. The animal alters the coloration, texture, and morphology of its skin to match the surrounding environment, making it difficult to discern (left). When startled, the octopus changes its appearance and becomes visible (right). B) A squid with mottled and partially transparent skin, which makes it difficult to distinguish from the rock in the background (left). After the squid alters the coloration of its skin, the animal becomes clearly visible (right). Part A) was reproduced with permission of Elsevier. Copyright 2007. 4

Figure 1.3. **Descriptions of the biophotonic organs in cephalopod skin.** A) A picture of cuttlefish skin that shows leucophores (white), chromatophores (yellow, red, and dark brown) and iridophores (green). B) A diagram of “typical” cephalopod skin that illustrates the optical functionality of leucophores, iridophores, and chromatophores. The leucophores primarily provide a white background, the iridophores primarily serve as dynamic Bragg reflectors, and the chromatophores primarily absorb and filter light. The picture shows two states on the left and the right (see the expanded cells and distinct ray traces), exemplifying the sophisticated means by which cephalopods change their coloration. Parts A) and B) were reproduced with permission of The Royal Society. Copyright 2012. 5

Figure 1.4. **Descriptions of iridophores and a chromatophores.** A) An illustration of an iridophore and its associated membrane-enclosed reflectin platelets, which alternate with extracellular space to form biological Bragg reflectors. The geometry and optical properties of the reflectors are modulated through a sophisticated signaling cascade. B) A microscope image of iridophores with different colorations. C) An illustration of a chromatophore and its encapsulated tethered pigment granule network. The architecture and optical properties of the pigment network are controlled by the radial muscle fibers. D) A picture of chromatophores in their punctate (dot-like) and expanded states. Parts A) and B) were reproduced with permission of the National Academy of Sciences, USA. Copyright 2013. Part C) was reproduced with permission of The Royal Society. Copyright 2014. Parts C) and D) were reproduced with permission of Springer. Copyright 2007. 6

Figure 1.5. Descriptions of the production, visible appearance, and functionality of a reflectin-based film. A) The procedure for flow coating reflectin films onto hard substrates. B) A reflectin film that featured a thickness gradient, which was produced by adjusting the tilt of the blade during fabrication. C) The corresponding reflectance spectra for the different regions of the film in B). Note that the coloration of the film was dictated by thin film interference. Parts A), B), and C) were reproduced with permission of Macmillan Publishers Ltd: Nature Materials. Copyright 2007. 7

Figure 1.6. Description of the production, appearance, and functionality of reflectin-based films upon the application of an exogenous stimulus. A) The procedure for fabrication of reflectin films on graphene oxide-modified substrates via doctor blading. B) A representative optical image of a reflectin film, for which the color was dictated by thin film interference. C) The change in thickness induced by acetic acid vapor for a reflectin film. D) The change in reflectance for a reflectin film as a function of time following the application of acetic acid vapor. Note that the initial reflectance spectrum could be recovered through removal of the acidic stimulus. Parts A) – D) were reproduced with permission of WILEY-VCH Verlag GmbH & Co. KGaA, Weinheim. Copyright 2013. 8

Figure 1.7. Description of an infrared-reflecting reflectin-based film A) A schematic of reflectin-coated tape in the absence of strain. B) An optical camera image of a camouflage fatigue overlaid with reflectin-coated tape, which was transparent in the absence of strain. C) The corresponding reflectance spectrum for the film in B). D) A schematic of reflectin-coated tape in the presence of strain. The application of a uniaxial strain to the tape altered the dimensions of the overlaid reflectin film. E) An optical camera image of the camouflage fatigue from B) after the application of strain to the reflectin-coated tape. Note that the tape became orange and opaque. F) The corresponding reflectance spectrum for the film in D), demonstrating a shift in the reflectance. Parts A) – F) were reprinted from reference 27. 10

Figure 1.8. Description of a color-changing elastomeric material A) An optical image of a silicone elastomer that contained covalently-attached spiropyran mechanophores in the absence of an applied strain (left), under a uniaxial strain of 200 % (middle), and after relaxation and illumination with green light (right). The applied strain caused a change in the coloration of the elastomer from pale yellow to blue, due to conversion of the spiropyrans into merocyanines. The relaxation of the strain and exposure to green light returned the mechanophores to their original state, as well as returned the coloration of the elastomer to yellow. B) Fluorescence microscope images of the film corresponding to the three situations in A), revealing the fluorescence of the merocyanines (middle). Parts A) and B) were reproduced with permission of Macmillan Publishers Ltd: Nature Communications. Copyright 2014. 11

Figure 1.9. Description of a dielectric elastomer-based artificial chromatophore. A) An image of a single artificial chromatophore, which was composed of a transparent dielectric elastomer layer stretched over a frame,

partially sandwiched between two transparent electrodes, and overlaid with a blue-colored gel. B) A schematic of the artificial chromatophore, for which the application of an electric field induced a change in both the geometry of the electrode and the color intensity of the overlaid gel. Part A) was reproduced with permission of IOP Publishing. Copyright 2012. 12

Figure 1.10. Images of innervated squid skin and of iridophores actuating upon the application of an electrical stimulus. A) A fluorescence image of innervated squid skin with the nerve fibers stained red. Note the proximity of the nerve fibers to the chromatophores and iridophores. B) An example of a single iridophore before (left) and after (right) nerve electrical stimulation. Note the change in color for the cell. C) An example of a fin iridophore cluster before (left) and after (right) electrical stimulation of the fin nerve. Note the change in color for the cell cluster. Parts A), B), and C) were reproduced with permission of The Royal Society. Copyright 2012. 14

Figure 1.11. Description of a multiplexed artificial chromatophore array. A) A schematic of a device that featured artificial chromatophores within multiple independent stacked layers. The three layers contained red (top), green (middle), and blue (bottom) electrode areas. Note that the layers could be electrically actuated independently. B) A schematic of a device for which the green and blue layers were actuated (top), the red and green layers were actuated (bottom left), and only the blue layer was actuated (bottom right). These figures are an artistic rendition of the schematics from reference 30. 15

Figure 1.12. Description an elastomer-based camouflaging device. A) Schematic of the top and side views of an elastomer layer that contained two different microfluidic channel networks. B) An image of the layer from A), for which one channel was filled with a red dye solution. C) An image of the layer from A), for which one channel was filled with a blue dye solution. D) An image of the layer from A), for which different channels were filled with red and blue dye solutions. E) Images of a microfluidic layer before (top) and after (bottom) injection of dye dispersions with different gray shades. The dispersions allowed the layer to match the appearance of the background rocks. F) Infrared camera images of the microfluidic layer from E) before (top) and after (bottom) injection of dye dispersions with different temperatures. The dispersions allowed the layer to stand out from its thermal environment. G) Images of an elastomer layer that was integrated with a pneumatically actuated soft robot. The robot was distinguishable from a red leaf background before injection of a dye solution (top) and blended into the red leaf background after injection of a dye solution (bottom). Parts A) – G) were reproduced with permission of The American Association for the Advancement of Science. Copyright 2012. 16

Figure 1.13. Description of a hyperelastic light-emitting capacitor. A) A schematic of the hyperelastic light-emitting capacitor, which consisted of an electroluminescent phosphor-containing layer sandwiched between two ionically-conducting polyacrylamide electrodes and encapsulated in a flexible silicon housing. B) A picture of a multi-pixel display comprised of arrayed capacitors.

The display emitted blue light upon application of an electric field (actuation). C) A picture of a multi-pixel display comprised of arrayed capacitors. The entire eight by eight pixel array was actuated and emited orange light. D) A picture of the display from (C), for which a six by six subset of the pixel array was actuated and emitted orange light. E) A picture of the display from C), for which a three by three subset of the pixel array was actuated and emitted orange light. Parts A) – E) were reproduced with permission of The American Association for the Advancement of Science. Copyright 2016. 17

Figure 1.14. Description of flexible, thermoresponsive multiplexed array. A) A schematic of a multilayer unit cell that incorporated essential design features found in cephalopod skin. The unit cells consisted of a thermochromic color-changing dye embedded in a polymer matrix, in analogy to a chromatophore; a thin silver layer as a bright white background, in analogy to a leucophore; a silicon diode heating element as an actuator, in analogy to the chromatophores' muscle fibers; and a silicon photodiode as a light sensor, in analogy to photoresponsive opsin-containing functional units. B) An optical image of a thermochromic equivalent to a chromatophore. C) An optical image of the silver layer and the silicon diode. D) An optical image of the diode. E) An optical image of a photodiode and an associated blocking diode for multiplexing. F) An illustration of an interconnected unit cell array in a complete artificial adaptive camouflage skin. G) An optical image of an interconnected unit cell array in a complete artificial adaptive camouflage skin. H) An image of a bent device that was actuated to display the text "UoI." I) Schematics and corresponding optical images of devices illuminated with light, which stimulated the photodiodes and induced a coloration change from black to white. As a shadow mask moved the light to different locations, the artificial camouflage skins were able to independently adapt their pattern to match the constantly changing position of the incident light. Parts A) – I) were reproduced with permission of the National Academy of Sciences, USA. Copyright 2014.. 19

Figure 1.15. Image of an octopus extending its tentacle and of an octopus expanding the papillae around its eye. A) A picture of an octopus and bait positioned at opposite ends of a glass tube, with the animal reaching for the bait (left). After the bait is moved further away, the octopus attempts to reach the bait by extending its arm to twice the original length (right). B) A picture of an octopus with flat skin around its eye (left). The octopus extends papillae to texture the skin (right). Part A) was reproduced with permission of Elsevier. Copyright 2013. Part B) was reproduced with permission of WILEY PERIODICALS, INC. Copyright 2013. 21

Figure 1.16. Description of an inverted, artificial chromatophore. A) A schematic of an "inverted" artificial chromatophore, which consisted of a central region overlaid with a blue-colored gel layer and surrounded by an annular electrode (left). The application of an electric field induced a change in the geometry and color intensity of the central region, as well as radial buckling/wrinkling of the surrounding electrode's surface (right). B) An image of

an "inverted" artificial chromatophore before (left) and after (right) electrical actuation. The device displayed a change in geometry and color intensity, as well as radial buckling/wrinkling of the central region of the surrounding electrode upon application of an electric field. Part B) was reproduced with permission of IOP Publishing. Copyright 2012. 22

Figure 1.17. Description of an electromechanochemically responsive material. A) A schematic of the electromechanochemically responsive structure, which consisted of a thin metal foil, a rigid protective insulator, a buffer elastomer layer, an electromechanochemically responsive elastomer layer, and a conductive salt solution electrode. B) A schematic of the structure from A), wherein the application of electric fields above material-specific critical values led to the formation of wrinkles. C) A schematic of the system from A), wherein the application of even larger electric fields led to the formation of craters. D) Optical microscope images of an initially flat elastomer layer for which applied electric fields of increasing magnitude induced surface texturing (the formation of craters). E) Fluorescence microscope images of the layer from D) showing that deformation around the crater edges locally converted the spiropyrans to fluorescent merocyanines. F) A schematic of a prestretched electromechanochemically responsive elastomer film (left). An optical microscope image of a prestretched film for which an electric field induced the formation of trenches (middle). A fluorescence microscopy image of the prestretched film demonstrating that the edges of the trenches were fluorescent (right). G) A schematic of an electromechanochemically responsive elastomer film with an obstacle embedded in the underlying buffer substrate (left). An optical microscope image of the film for which an electric field induced deformation along the contour of the obstacle (middle). A fluorescence microscopy image of the deformed film, which demonstrated that the edges of the obstacle were fluorescent (right). Parts A) – G) were reproduced with permission of Macmillan Publishers Ltd: Nature Communications. Copyright 2014. 23

Figure 1.18. Description of a hyperelastic light-emitting capacitor. A) Optical images of a hyperelastic light-emitting capacitor under different applied engineering strains. As the device was stretched to approximately five times its original length (left to right), the functionality was maintained, and the intensity increases in predictable fashion. B) A multi-pixel blue light-emitting display that was deformed by wrapping around a finger. C) A multi-pixel blue light-emitting display that was deformed by folding. D) A multi-pixel blue light-emitting display that was deformed by rolling. E) A deformed multi-pixel orange light-emitting display for which a subset of its pixels was actuated. Parts A) – E) were reproduced with permission of The American Association for the Advancement of Science. Copyright 2016. 25

Figure 1.19. Description of a proposed, adaptive garment. A) A picture of Under Armour's "Future Girl," who is in the process of donning a garment that adapts its size and shape to conform to the body of the wearer. B) A picture of the adaptive garment's wrist-mounted control and monitoring panel. C) The panel can

actuate the garment and change its coloration from gray (left) to blue (right). Parts A) – C) were reproduced with permission from Under Armour. 27

Figure 2.1. DLS Trace of of Reflectin A1 in solution. A representative dynamic light scattering spectrum obtained for a solution of RfA1.................................. 40

Figure 2.2. **DXMS exchange map for Reflectin A1.** The proton/deuteron exchange map for the RfA1 sequence after 10 s (top) and 30 s (bottom) of exposure to deuterium oxide. The rainbow color code (right) indicates the percent deuteration for each residue, which was calculated as the average over all peptides containing that residue. The black ovals correspond to the six conserved motifs of RfA1, as defined by Morse and co-workers.[18,21] 43

Figure 2.3. Illustration of a typical SAXS experiment. A schematic of a small-angle X-ray scattering experiment for RfA1 in solution. The incident X-rays are scattered by the solution-dispersed macromolecules, yielding a 2D pattern (data for RfA1 is shown)... 45

Figure 2.4. Log-lin plot showing data and simulated model fit for a SAXS experiment for solution phase reflectin. A 1D plot of the scattering intensity $I(q)$ versus the scattering vector q obtained for a solution of RfA1. The black circles represent the experimental data, and the red line represents the simulated scattering intensity profile... 47

F**igure 2.5. Guinier Plot showing a fit to the linear region, a Porod plot showing a fit to the linear region, a Kratky plot, and a distribution function. The plots correspond to the scattering intensity profile in Figure 2.4. A)** A Guinier plot of the integrated scattering intensity I(q) versus the square of the scattering vector q^2. The black dots represent the experimental data, and the red line represents a fit of a linear region of the data at low q. **B)** A Porod plot of the integrated scattering intensity times the fourth power of the scattering vector I(q) x q^4 versus the scattering vector q. The black dots represent the experimental data, and the red line represents a linear fit of the data. **C)** A Kratky plot of the integrated scattering intensity times the square of the scattering vector I(q) x q^2 versus the scattering vector q. **D)** A representative plot of the distance distribution P(r) versus the distance r. 49

Figure 2.6. Scanning electron microscopy characterization of substrate bound reflectin nanoparticles A) A representative scanning electron microscopy images of RfA1 nanoparticles on a silica substrate. The red squares indicate RfA1 nanoparticle multimers (dimers). The blue square indicates an individual RfA1 nanoparticle that was imaged at increased magnification. B) A close- up high-resolution scanning electron microscopy image of the RfA1 nano- particle enclosed by the blue square in (A).. 51

Figure 2.7. Illustrated description a typical in situ GISAXS experiment. A) A schematic of a grazing incidence small angle X-ray scattering experiment for an

RfA1 film. The incident X-rays are scattered by substrate-confined aggregated macromolecules, yielding a 2D pattern (data for RfA1 is shown). 53

Figure 2.8. Plot showing experimental data and simulated scattering profiles from an in situ GISAXS experiment of reflectin self-assembly. A 1D plot of the grazing incidence small- angle X-ray scattering intensity $I_G(q)$ versus the scattering vector q_Y obtained at different times during the self-assembly/formation of a film from RfA1 nanoparticles. The measurements were obtained at 3 (blue), 7 (green), 11 (purple), and 23 (brown) min after initiation of assembly. The circles represent the experimental data, and the lines represent the simulated scattering intensity profiles. The green, purple, and brown curves have been offset vertically for clarity.. 55

Figure 2.9. A 1D plot of the grazing incidence small-angle X-ray scattering intensity $I_G(q)$ versus the scattering vector q_y obtained for an RfA1 film before and after hydration. The orange circles represent the experimental data obtained before hydration, and the solid orange line represents the simulated scattering intensity profile. The red circles represent the experimental data obtained after hydration, and the solid red line represents the simulated scattering intensity profile. The orange curve has been offset vertically for clarity............. 58

Figure 2.10. A schematic of a grazing incidence wide-angle X-ray scattering experiment for an RfA1 film. The incident X-rays are scattered by substrate-confined aggregated macromolecules, yielding a 2D pattern (the data for RfA1 are shown)... 60

Figure 2.11. A 1D plot of the grazing incidence wide-angle X-ray scattering intensity $I_W(q)$ versus the scattering vector q obtained for a RfA1 film and for a blank silicon dioxide substrate. Note the absence of any obvious peaks in the trace corresponding to the silicon dioxide substrate. The measurement was performed under conditions identical to those used for collection of the data in **Figure 2.14**. 61

Figure 2.12. Illustration of the hierarchical organization of RfA1 in solution and in films. When dispersed in solution, RfA1 aggregates into interacting nanoparticles with an asymmetric prolate (elongated) geometry. When self-assembled into films, the RfA1 nanoparticles still interact and adopt an oblate (flattened) geometry, which changes slightly upon the application of a stimulus (an increase in relative humidity leading to hydration). 63

Figure 3.1 An illustration of a proposed approach to studying the reflectin family and synthesizing reflectin variants thereof. The RfA1 protein is composed of six similar amino acid sequences, which may be synthesized, characterized, and recombined into reflectin peptide mutants.. 79

LIST OF TABLES

Table 2.1 A table stating the equation and listing the values used to develop a simulated SAXS profile. The equation and corresponding parameters employed to generate the simulated scattering curve in **Figure 2.4**. The equation and parameter definitions were adapted from the protocols in reference 56. ………. 50

Table 2.2 A table stating the equation and listing the values used to develop a simulated GISAXS profile for a reflectin self-assembly experiment. The equation and corresponding parameters employed to generate the simulated scattering curves in **Figure 2.9**. The equation and parameter definitions were adapted from the protocols in reference 56…………………………………….. 57

Table 2.3 A table stating the equation and listing the values used to develop a simulated GISAXS profile to model geometrical changes of a reflectin film upon stimulus. The equation and corresponding parameters employed to generate the simulated scattering curves in Figure 2.9. The equation and parameter definitions were adapted from the protocols in reference 56…………………… 59

AKNOWLEDGMENTS

I thank Professor Alon Gorodetsky for his guidance during my pursuit of a Masters degree. I would also like to thank Professor Zuzanna Siwy for her inalienable patience, warmth, and mentorship during my tenure at UCI and for acting as a member of my thesis committee. I also thank Professor Jun Allard for his insight into my work, for lending me his sage input through my research, and for acting as a member of my thesis committee.

I would also like to thank the other members of the Gorodestky group past and present for their invaluable friendship. Further, I would like thank Dr. Steven Jim for his daily and enduring support.

Finally, I thank my mother, father, sisters, family, and friends for their love, without whom none of this would be possible.

Chapter 1 of this thesis is a reprint of the material as it appears in Chemistry of Materials. The co-authors listed in this publication directed and supervised research which forms the basis for the thesis. Author Contributions: P. L., and G. A. A. designed research; P. L., K. R., L. E. M., N. K. L, and V. D. Y performed research; and P.L., K.R., L. E. M., N. K. L, V. D. Y., and G. A. A. wrote the paper. Chapter 2 of this thesis is a reprint of the material as it appears in Advanced Materials. Author contributions: N. K. L., L. Q., G. E. D., B.S., Z.C., G. A. A. designed research; N. K. L., P. L., L. E. M., L. Q., V. D. Y., M. B., S. B. A. A., L. S., P. M. E., M. N., K. P. J., A. M. J., and R. V. A. performed research; N. K. L., K. R., L. Q., Z. C., and B. S. analyzed data; N. K. L., and G. A. A., wrote the paper

ABSTRACT OF THE THESIS

Towards Understanding a Dynamic Cephalopod Protein Reflectin

Kyle Liam Naughton

Master of Science in Physics

University of California, Irvine, 2017

Biomaterials have the unique ability to actively respond to environmental stimuli for the purpose of motility, metabolism, and, in the case of some animals, camouflage. Proteins often serve these critical biological functions because of their multi-scale, hierarchical functionality and specific chemical activity. Cephalopods- octopus, cuttlefish, and squid- posses a unique family of proteins known as reflectins which imbue these creatures with their remarkable camouflage abilities. The cephalopod, therefore, may serve both as a source of inspiration towards developing new materials and a subject of study to better understand the activity and self-assembly of proteins in general. Herein, a selection of cephalopod-inspired materials is reviewed from the literature. The merits, unique properties, and challenges of developing these dynamic materials are discussed. Next, an exotic protein implicated as the active material in biophotonic organelles of a loliginid squid known as reflectin isoform A1 (RfA1) is characterized. By deploying a variety of advanced X-ray scattering techniques and a suite of biophysical characterizing methods, the geometry and self-assembly of this protein is observed both in the solvated and solid state. Altogether, this work holds relevance towards fundamentally understanding the reflectin protein family and towards developing the field of self-actuating, reconfigurable materials.

CHAPTER 1 Dynamic Materials Inspired by Cephalopods[†]

1.1 Abstract

The related concepts of disguising an object or physically changing it to resemble something entirely different have long captivated the human imagination. Although such notions are seemingly derived from fables and science fiction, cephalopods have perfected analogous capabilities over millions of years of natural evolution. Consequently, these invertebrates have emerged as exciting sources of inspiration for futuristic adaptive camouflage and shape-shifter-like technologies. Herein, we provide an overview of selected literature examples that have used cephalopods as models for the development of novel adaptive materials, devices, and systems. We in turn highlight some significant remaining challenges and potential future directions for such studies. Through this perspective, we hope to stimulate additional dialogue and continued scientific exploration within the area of cephalopod-inspired dynamic materials.

1.2 Introduction

The related concepts of adaptive camouflage (disguising an object in real time such that it cannot be detected) and shapeshifting (physically transforming an entity into something entirely different) have captivated the human imagination

---

[†] This chapter appears in the published article of the same title. Phan, L.; Kautz, R.; Leung, E. M.; Naughton, K. L.; Van Dyke, Y.; Gorodetsky, A.A.; Dynamic Materials Inspired by Cephalopods, *Chem. Mater.,* **2016**, *28*, 6804–6816.

and influenced popular culture since classical antiquity.[1-4] For example, Greek and Roman mythology contained many famous examples of the ancient gods shapeshifting into animals or people, such as the tale of Vertumnus (Figure 1.1A) taking the form of an old woman in order to woo Pomona (Figure 1.1B).[1]

Figure 1.1. **Illustrations of camouflage through history.** A) A painting by Giuseppe Arcimboldo of Vertumnus, the Roman mythological god of seasons, who is able to alter his form at will. B) A painting by Paulus Moreelse, in which Vertumnus has changed form into an old woman to woo Pomona. C) A medieval woodcut by Hans Weiditz of a human who has transformed into a wolf and is attacking two men. Part A) painting Public domain was reproduced via Wikimedia Commons. Part B) painting Public domain was reproduced via Wikimedia Commons. Part C) woodcut Public domain was reproduced via Wikimedia Commons.

The fascination with changing form continued during the Middle Ages, when lycanthropy (the transformation of a human into a wolf or wolf-like creature) emerged as a widespread theme in European folklore and superstition (Figure 1.1C).[2] In the modern era, such classic ideas have manifested themselves via science fiction books and movies; for instance, the characters of Mystique and Beast from the X-men series of comic books and movies embodied the concepts of adaptive camouflage and shapeshifting.[3,4] Although these notions once may have seemed fantastic, the accelerated pace of technological innovation has enabled scientists to envision technologies that would make such ideas a routine part of daily life.

Remarkably, the concepts of adaptive camouflage and shapeshifting reach beyond fables and science fiction – over millions of years of natural evolution, cephalopods (e.g, squid, octopuses, and cuttlefish) have developed and refined these capabilities for communication and disguise.[5-11] For example, Figure 1.2A shows a common octopus on a seaweed- and algae-covered rock.[10] The animal can blend almost perfectly into its environment by matching the surrounding patterning, color, shape, and texture (Figure 1.2A left) and only becomes clearly visible upon being disturbed (Figure 1.2A, right).[10] Other cephalopods, such as the squid in Figure 1.2B, are capable of equally striking feats.[11] When swimming in front of a rocky background, the squid nearly disappears due to its mottled and partially transparent skin (Figure 1.2, left) and is only easily distinguishable when its skin turns dark and relatively uniform (Figure 1.2B, right).[11] Due to such visually stunning demonstrations, cephalopods have emerged as an exciting source of inspiration for the development of adaptive color- and shape-changing technologies.

To understand (and ultimately emulate) the capabilities of cephalopods, it is instructive to consider their generalized skin architecture and morphology (note that the exact arrangement varies among different species) (Figure 1.3).[9] “Typical” cephalopod skin consists of multiple layers containing optically active cells known as leucophores, iridophores, and chromatophores, which work in concert but possess distinct primary functions (Figure 1.3).[5,9] The leucophores serve as diffuse reflectors that scatter incident light, the iridophores serve as dynamic Bragg stacks that reflect light of specific wavelengths, and the chromatophores serve as selective spectral filters that modulate the absorbance/transmission of light (note that the cell types and their specific functionality also may vary among different species) (Figure 1.3B).[9,12-20]

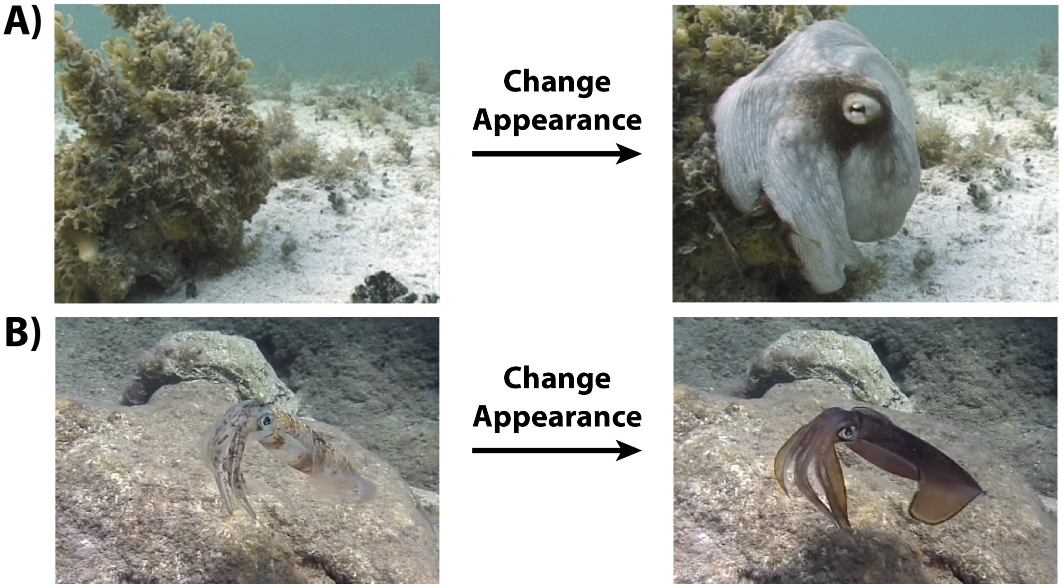

Figure 1.2. Optical Images of cephalopods changing appearance to blend into their environment A) A camouflaged octopus positioned on a rock. The animal alters the coloration, texture, and morphology of its skin to match the surrounding environment, making it difficult to discern (left). When startled, the octopus changes its appearance and becomes visible (right). B) A squid with mottled and partially transparent skin, which makes it difficult to distinguish from the rock in the background (left). After the squid alters the coloration of its skin, the animal becomes clearly visible (right). Part A) was reproduced with permission of Elsevier. Copyright 2007.

For some cephalopods, iridophores and chromatophores are controlled via an extensive network of embedded nerve fibers, which effectively multiplexes the cells and connects them to the central nervous system.[16,20] Moreover, many cephalopods can often change the physical form and shape of their skin, all without negatively affecting the embedded cells' optical functionality.[9,21-24] Thus, cephalopod skin essentially functions as a sophisticated three-dimensional adaptive display, with a combination of switchable vivid coloration, hierarchical multiplexing and pixelation, and precise shape and texture modulation that remains unrivaled both in the animal kingdom and among modern optical devices.

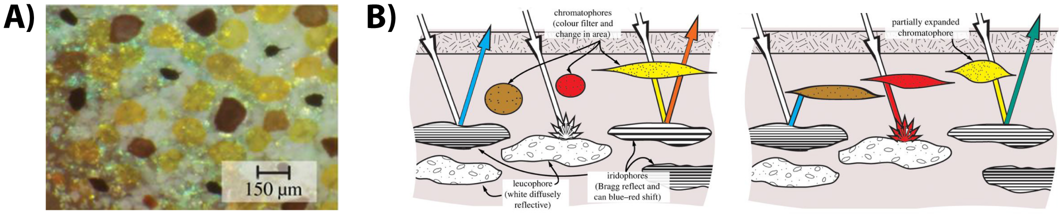

Figure 1.3. **Descriptions of the biophotonic organs in cephalopod skin.** A) A picture of cuttlefish skin that shows leucophores (white), chromatophores (yellow, red, and dark brown) and iridophores (green). B) A diagram of "typical" cephalopod skin that illustrates the optical functionality of leucophores, iridophores, and chromatophores. The leucophores primarily provide a white background, the iridophores primarily serve as dynamic Bragg reflectors, and the chromatophores primarily absorb and filter light. The picture shows two states on the left and the right (see the expanded cells and distinct ray traces), exemplifying the sophisticated means by which cephalopods change their coloration. Parts A) and B) were reproduced with permission of The Royal Society. Copyright 2012.

In this perspective, we provide an overview of recent cephalopod-inspired studies, which can be viewed as preliminary steps towards realizing adaptive camouflage and shapeshifter-like technologies. First, we highlight various materials and devices that reversibly change their coloration. Subsequently, we describe integrated systems that are capable of sophisticated patterning. In turn, we present materials that alter both their color and texture/shape. Finally, we conclude with an overview of some potential applications and key remaining challenges. Here, we note that natural systems have evolved a fantastically diverse array of advanced photonic structures,[25-27] which have led to an impressive number of efforts seeking to understand and emulate their functionality.[28-30] As such, our perspective in no way constitutes an exhaustive review but rather presents specific excerpts from a limited number of selected case studies (which were all explicitly inspired by cephalopods). Through our discussion of several illustrative examples, we hope to stimulate additional dialogue and further work in the exciting emerging area of cephalopod-inspired dynamic materials.

1.3 Discussion

1.3.1 Switchable Coloration

Coloration changes in cephalopod skin are actuated through a diverse combination of mechanisms. As one example, Figure 1.4A shows a schematic of a squid iridophore, which is actuated in part through a chemical stimulus.[14] The membrane of this cell folds to encompass platelets from a protein called reflectin, and these membrane-enclosed layers alternate with extracellular space to form Bragg reflector-like structures (Figure 1.4A).

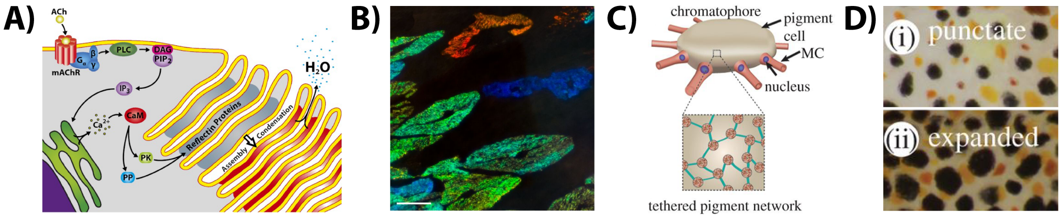

Figure 1.4. **Descriptions of iridophores and a chromatophores.** A) An illustration of an iridophore and its associated membrane-enclosed reflectin platelets, which alternate with extracellular space to form biological Bragg reflectors. The geometry and optical properties of the reflectors are modulated through a sophisticated signaling cascade. B) A microscope image of iridophores with different colorations. C) An illustration of a chromatophore and its encapsulated tethered pigment granule network. The architecture and optical properties of the pigment network are controlled by the radial muscle fibers. D) A picture of chromatophores in their punctate (dot-like) and expanded states. Parts A) and B) were reproduced with permission of the National Academy of Sciences, USA. Copyright 2013. Part C) was reproduced with permission of The Royal Society. Copyright 2014. Parts C) and D) were reproduced with permission of Springer. Copyright 2007.

The reversible phosphorylation of reflectin induces platelet condensation/dehydration, changing the spacing, thickness, and refractive index of the layers and thus altering the dimensions of the Bragg reflectors. This reversible process allows the iridophores to dynamically modulate their apparent color (Figure 1.4B).[14] As another example, Figure 4C shows a schematic of a cuttlefish chromatophore, which is actuated in part through a mechanical stimulus.[17] The cell is ringed by radial muscle fibers and encompasses sacs filled with a network of pigment granules, which contain pigments, reflectins, and crystallins (Figure 1.4C).[17] The muscle fibers expand the red, yellow, or brown chromatophores from barely visible spherical points to thin colored plates, altering the architecture, absorbance, and luminescence of the embedded granule network and enabling the cells to serve as spectral filters (Figure 1.4D).[17] The functionality of both of these cell types makes them attractive as models for artificial color-changing materials, devices, and systems.

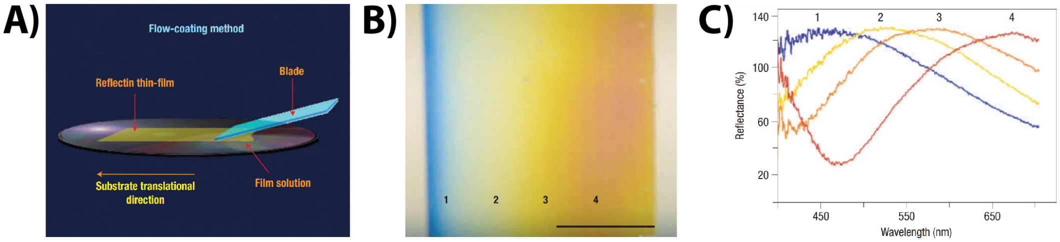

Figure 1.5. Descriptions of the production, visible appearance, and functionality of a reflectin-based film. A) The procedure for flow coating reflectin films onto hard substrates. B) A reflectin film that featured a thickness gradient, which was produced by adjusting the tilt of the blade during fabrication. C) The corresponding reflectance spectra for the different regions of the film in B). Note that the coloration of the film was dictated by thin film interference. Parts A), B), and C) were reproduced with permission of Macmillan Publishers Ltd: Nature Materials. Copyright 2007.

Kramer and coworkers drew inspiration from reflectin platelets in iridophores and studied protein-based thin films and microstructures.[31] For this purpose, the authors used the protein reflectin, which had been shown to play a crucial role in the optical functionality of iridophores.[14,15] Figure 1.5A illustrates the general film fabrication procedure, which entailed flow coating reflectin over a blade onto an underlying substrate. The process yielded films for which the coloration was determined by their thickness and thin film interference (Figure 1.5B and Figure 1.5C). Consequently, the authors demonstrated that water vapor-induced swelling reversibly modulated the films' coloration, albeit across a relatively narrow range. Furthermore, the authors self-assembled reflectin into fibers and diffraction gratings, which held potential for more advanced photonic applications. These seminal experiments highlighted the promise of materials that occur naturally in cephalopods for applications in dynamic color-changing optical devices.

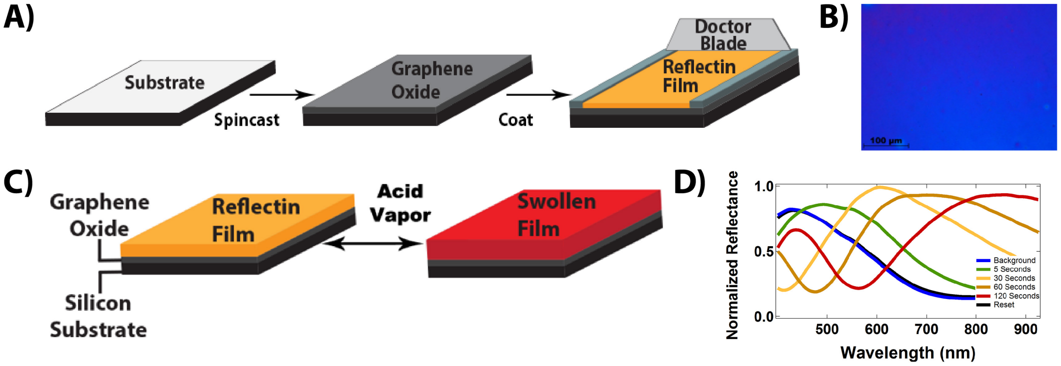

Figure 1.6. Description of the production, appearance, and functionality of reflectin-based films upon the application of an exogenous stimulus. A) The procedure for fabrication of reflectin films on graphene oxide-modified substrates via doctor blading. B) A representative optical image of a reflectin film, for which the color was dictated by thin film interference. C) The change in thickness induced by acetic acid vapor for a reflectin film. D) The change in reflectance for a reflectin film as a function of time following the application of acetic acid vapor. Note that the initial reflectance spectrum could be recovered through removal of the acidic stimulus. Parts A) – D) were reproduced with permission of WILEY-VCH Verlag GmbH & Co. KGaA, Weinheim. Copyright 2013.

Phan and coworkers also drew inspiration from reflectin platelets in iridophores and investigated protein-based color-changing coatings on hard substrates (in analogy to the work of Kramer and coworkers).[32] Figure 1.6A illustrates the general film fabrication procedure, which consisted of functionalizing the substrate with graphene oxide and then covering the surface with the stimuli-responsive protein reflectin. The process yielded films like the one shown in Figure 1.6B, for which the coloration was dictated by the thickness. The authors next modulated the films' apparent color through exposure to acetic acid vapor, which induced substantial swelling due to changes in intraprotein electrostatic interactions (Figure 1.6C). By controlling this chemical stimulus, the authors were able to reversibly tune the films' reflectance across the entire visible spectrum and even into the near infrared (Figure 1.6D). Notably, the films functioned as a rudimentary form of active infrared camouflage, disguising objects from visualization under illumination with infrared light. These experiments demonstrated functionality not necessarily intended by nature, as well as a large dynamic coloration range, for protein-based coatings.

Phan and coworkers subsequently followed up on their initial experiments and studied color-changing coatings on conformable adherent substrates.[33] The authors first adapted their fabrication procedures for flexible substrate materials, forming reflectin films on graphene oxide-coated fluorinated ethylene propylene tape (Figure 1.7A). In turn, they applied the tape to standard camouflage fabrics as stickers, which were relatively difficult to distinguish from the background (Figure 1.7B). The initial unactuated stickers were transparent and featured peak reflectances in the near infrared (Figure 1.7C). However, upon mechanical actuation (uniaxial stretching), the thickness of the "stickers" and the overlaid reflectin films decreased due to the Poisson effect (Figure 1.7D). The actuated stickers thus acquired an opaque orange color (Figure 1.7E) and featured peak reflectances in the visible (Figure 1.7F), making them straightforward to identify. Here, the authors again used their systems as active infrared camouflage, noting the stickers' potential deployment flexibility. These experiments represented a straightforward method for the integration of simple mechanically-actuated systems with fabrics.

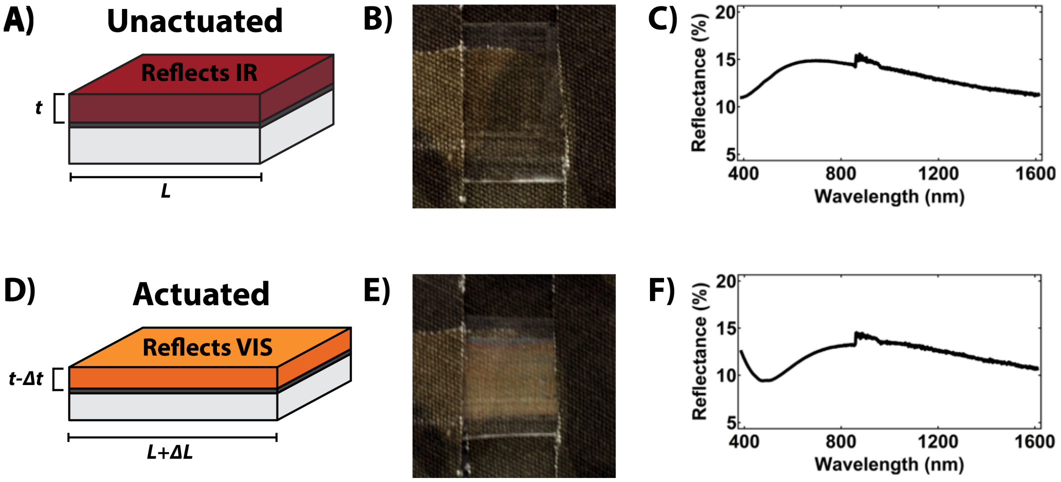

Figure 1.7. Description of an infrared-reflecting reflectin-based film A) A schematic of reflectin-coated tape in the absence of strain. B) An optical camera image of a camouflage fatigue overlaid with reflectin-coated tape, which was transparent in the absence of strain. C) The corresponding reflectance spectrum for the film in B). D) A schematic of reflectin-coated tape in the presence of strain. The application of a uniaxial strain to the tape altered the dimensions of the overlaid reflectin film. E) An optical camera image of the camouflage fatigue from B) after the application of strain to the reflectin-coated tape. Note that the tape became orange and opaque. F) The corresponding reflectance spectrum for the film in D), demonstrating a shift in the reflectance. Parts A) – F) were reprinted from reference 27.

Wang and coworkers drew inspiration from the mechanical actuation of chromatophores and investigated elastomers with mechanoresponsive coloration (in an alternative approach to the one of Phan and coworkers).[34] The authors prepared cross-linked silicone elastomers containing the covalently-attached mechanophore spiropyran. In the absence of a mechanical stimulus, the elastomers possessed a pale yellow color (Figure 1.8A, left). However, the application of a sufficient uniaxial strain induced a ring-opening reaction, transforming the spiropyran to a merocyanine and changing the color of the elastomers to blue (Figure 1.8A, middle). The relaxed elastomers were returned to their original state through irradiation with green light, which induced a ring-closing reaction and converted the merocyanine back to a spiropyran (Figure 1.8, right). Notably, due to the fluorescence of the embedded molecules, the authors

were able to monitor the entire reversible conversion process with fluorescence microscopy (Figure 1.8B). These experiments showcased the coupling of

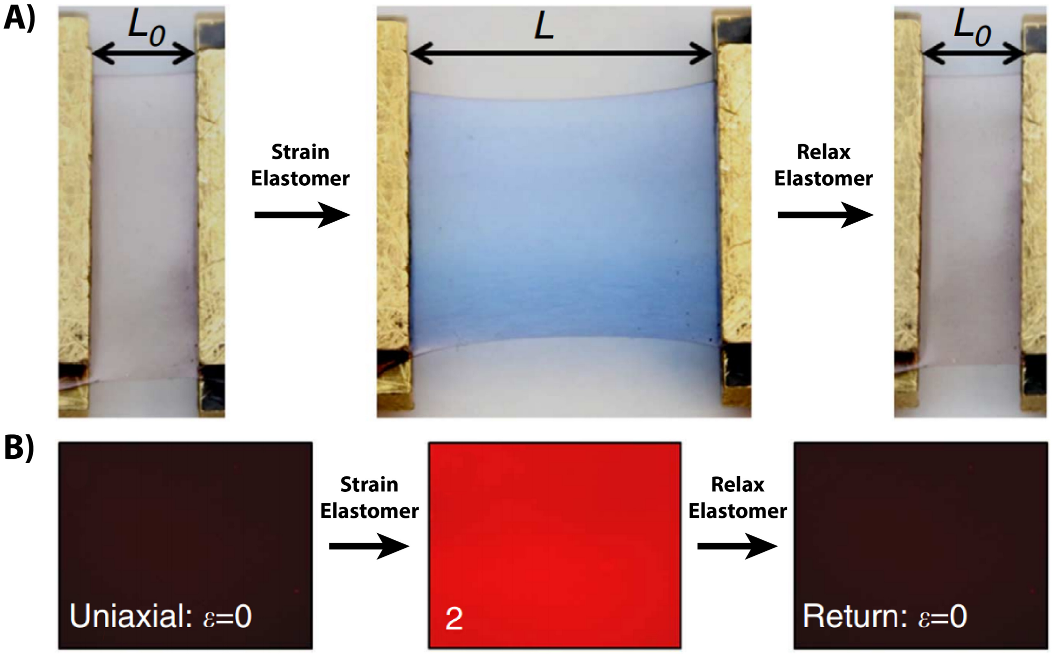

Figure 1.8. Description of a color-changing elastomeric material A) An optical image of a silicone elastomer that contained covalently-attached spiropyran mechanophores in the absence of an applied strain (left), under a uniaxial strain of 200 % (middle), and after relaxation and illumination with green light (right). The applied strain caused a change in the coloration of the elastomer from pale yellow to blue, due to conversion of the spiropyrans into merocyanines. The relaxation of the strain and exposure to green light returned the mechanophores to their original state, as well as returned the coloration of the elastomer to yellow. B) Fluorescence microscope images of the film corresponding to the three situations in A), revealing the fluorescence of the merocyanines (middle). Parts A) and B) were reproduced with permission of Macmillan Publishers Ltd: Nature Communications. Copyright 2014.

mechanical and chemical effects for the induction of coloration changes in elastomeric materials.

Rossiter and coworkers also drew inspiration from the mechanical actuation of chromatophores and studied polymer-based artificial variants of these cells (in another alternative strategy).[35] The authors fabricated their devices from dielectric elastomers, a class of materials for which the application of an electric field induces transverse thickness compression and planar areal expansion.[35,36] The artificial chromatophores consisted of a clear polyacrylate dielectric elastomer layer sandwiched by two transparent, compliant electrodes and overlaid with a blue-colored soft gel (Figure 1.9A). Prior to actuation, the appearance of the device was dictated by the initial size of the electrodes and the color of the overlaid gel (Figure 1.9B, left), but after electrical actuation, the appearance of the device was determined by the applied transverse electric field, which increased the electrode active area and reduced the gel color intensity (Figure 1.9B, right). These experiments constituted an initial demonstration of cephalopod-inspired devices that were actuated electrically.

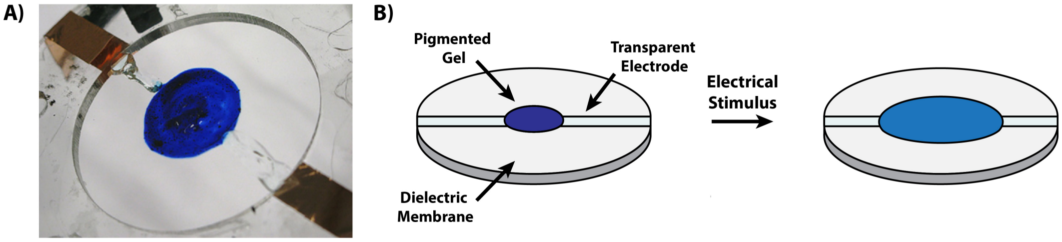

Figure 1.9. Description of a dielectric elastomer-based artificial chromatophore. A) An image of a single artificial chromatophore, which was composed of a transparent dielectric elastomer layer stretched over a frame, partially sandwiched between two transparent electrodes, and overlaid with a blue-colored gel. B) A schematic of the artificial chromatophore, for which the application of an electric field induced a change in both the geometry of the electrode and the color intensity of the overlaid gel. Part A) was reproduced with permission of IOP Publishing. Copyright 2012.

3.1.1 Hierarchical Multiplexing and Pixelation

Many cephalopods control the appearance of their skin at both the local and global levels via an interconnected network of embedded nerve fibers.[16,20] As an example, Figure 1.10A shows a fluorescence microscopy image of squid fin skin, for which the nerve fibers are stained red with a fluorescent dye.[20] The image demonstrates that the nerves are highly branched and situated near the iridophores and chromatophores (or contact them directly). Remarkably, direct electrical stimulation of the nerves triggers coloration changes of the innervated cells, as shown for both individual iridophores (Figure 1.10B) and entire iridophore clusters (Figure 1.10C).[20] Thus, the nerve fibers effectively serve to multiplex the three-dimensional network of color-changing elements that comprise the skin. Consequently, the general strategy employed by squid to hierarchically modulate their skin's appearance holds appeal for applications in autonomous multiplexed systems from independently addressable color-changing elements.

Rossiter and coworkers built upon their earlier experiments and investigated the optical functionality of devices from multiple artificial chromatophores.[36] Thus, the authors fabricated more advanced devices, which consisted of three distinct dielectric elastomer layers partially sandwiched by either red, green, or blue pigmented electrode areas and stacked on top of one another (Figure 1.11A). For this chromatophore cluster or pixel configuration, the layers could be addressed and electrically actuated independently. As an example, Figure 1.11B shows a schematic of a device that was cycled between different coloration states, wherein the green and blue layers were actuated (Figure 1.11B, top), the red and green layers were actuated (Figure 1.11B, bottom left), and only the blue layer was actuated (Figure 1.11B, bottom right). The authors modeled the coloration of such clusters when integrated into a large array, spaced precisely apart,

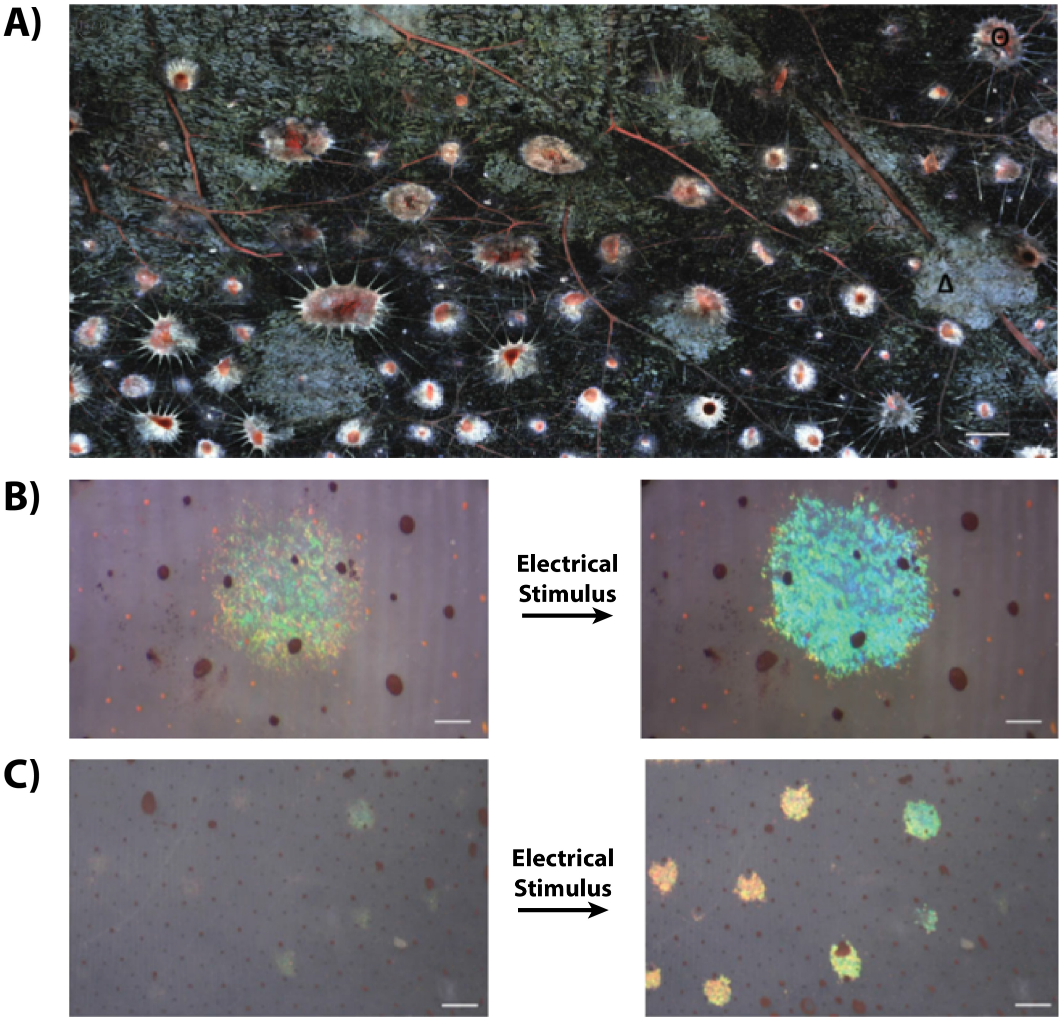

Figure 1.10. Images of innervated squid skin and of iridophores actuating upon the application of an electrical stimulus. A) A fluorescence image of innervated squid skin with the nerve fibers stained red. Note the proximity of the nerve fibers to the chromatophores and iridophores. B) An example of a single iridophore before (left) and after (right) nerve electrical stimulation. Note the change in color for the cell. C) An example of a fin iridophore cluster before (left) and after (right) electrical stimulation of the fin nerve. Note the change in color for the cell cluster. Parts A), B), and C) were reproduced with permission of The Royal Society. Copyright 2012.

multiplexed for arbitrary electrical triggering, and viewed from a distance. The theoretical modeling indicated that arrayed pixels would be capable of generating a wide range of colors. These experiments laid a conceptual foundation for the preparation of systems that use only simple elements to mimic a broad color palette.

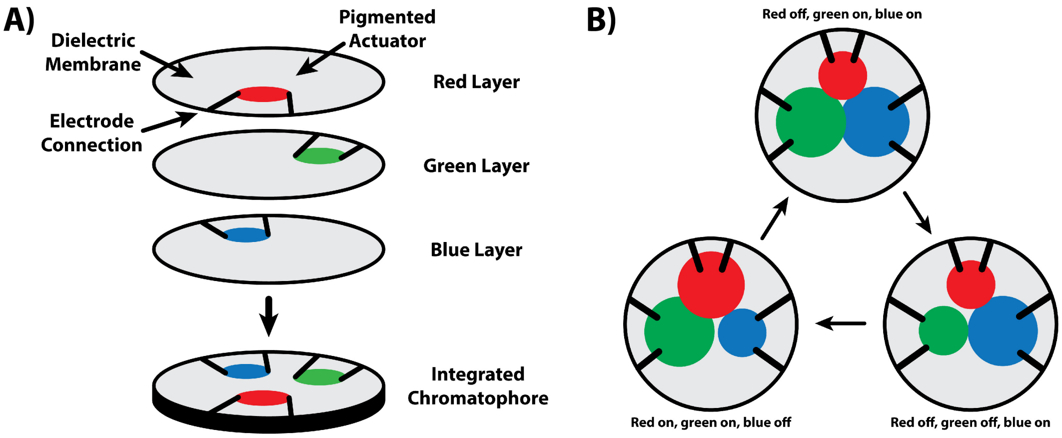

Figure 1.11. Description of a multiplexed artificial chromatophore array. A) A schematic of a device that featured artificial chromatophores within multiple independent stacked layers. The three layers contained red (top), green (middle), and blue (bottom) electrode areas. Note that the layers could be electrically actuated independently. B) A schematic of a device for which the green and blue layers were actuated (top), the red and green layers were actuated (bottom left), and only the blue layer was actuated (bottom right). These figures are an artistic rendition of the schematics from reference 30.

Morin and coworkers drew inspiration from the global color-changing abilities of cephalopod skin and studied a sophisticated integrated system that was capable of concealment in diverse settings.[37] For this purpose, the authors fabricated elastomer layers containing distinct networks of independently addressable microfluidic channels (Figure 1.12A). Through injection of distinct liquids into the channels, the layers' coloration and patterning could be changed in a predetermined fashion; Figure 1.12B, Figure 1.12C, and Figure 1.12D show the appearance of a layer for which one channel was filled with a red dye solution, one channel was filled with a blue dye solution, or two different channels were filled with red and blue dye solutions, respectively. The authors also demonstrated that layers filled with appropriate dye dispersions were capable of matching various backgrounds, such as rocks (Figure 1.12E). Moreover, through injection of solutions with controlled temperatures, the layers could be induced to either blend into or stand out against their thermal environments (Figure 1.12F). Notably, by integrating the microfluidic layers with pneumatically actuated soft robots, the authors manufactured mobile systems that exhibited identical

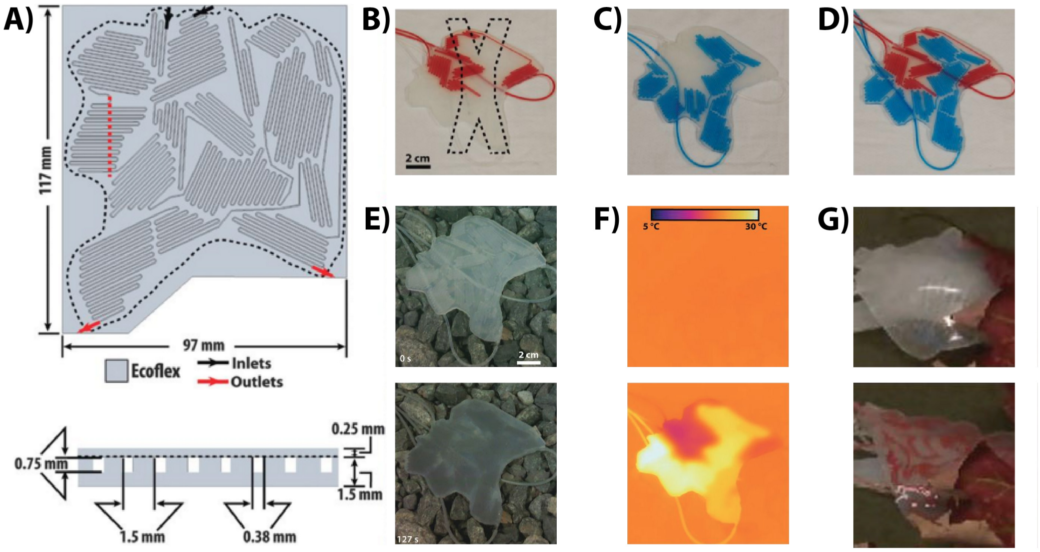

Figure 1.12. Description an elastomer-based camouflaging device. A) Schematic of the top and side views of an elastomer layer that contained two different microfluidic channel networks. B) An image of the layer from A), for which one channel was filled with a red dye solution. C) An image of the layer from A), for which one channel was filled with a blue dye solution. D) An image of the layer from A), for which different channels were filled with red and blue dye solutions. E) Images of a microfluidic layer before (top) and after (bottom) injection of dye dispersions with different gray shades. The dispersions allowed the layer to match the appearance of the background rocks. F) Infrared camera images of the microfluidic layer from E) before (top) and after (bottom) injection of dye dispersions with different temperatures. The dispersions allowed the layer to stand out from its thermal environment. G) Images of an elastomer layer that was integrated with a pneumatically actuated soft robot. The robot was distinguishable from a red leaf background before injection of a dye solution (top) and blended into the red leaf background after injection of a dye solution (bottom). Parts A) – G) were reproduced with permission of The American Association for the Advancement of Science. Copyright 2012.

camouflage capabilities. For example, Figure 1.12G shows a robot among leaves before it is filled with a dye solution (when it is clearly visible), as well as the same robot after being filled with a dye solution (when it is more difficult to discern from the background). Together, these experiments constituted a substantial advance with regard to mobile systems that adaptively emulate a wide range of environments.

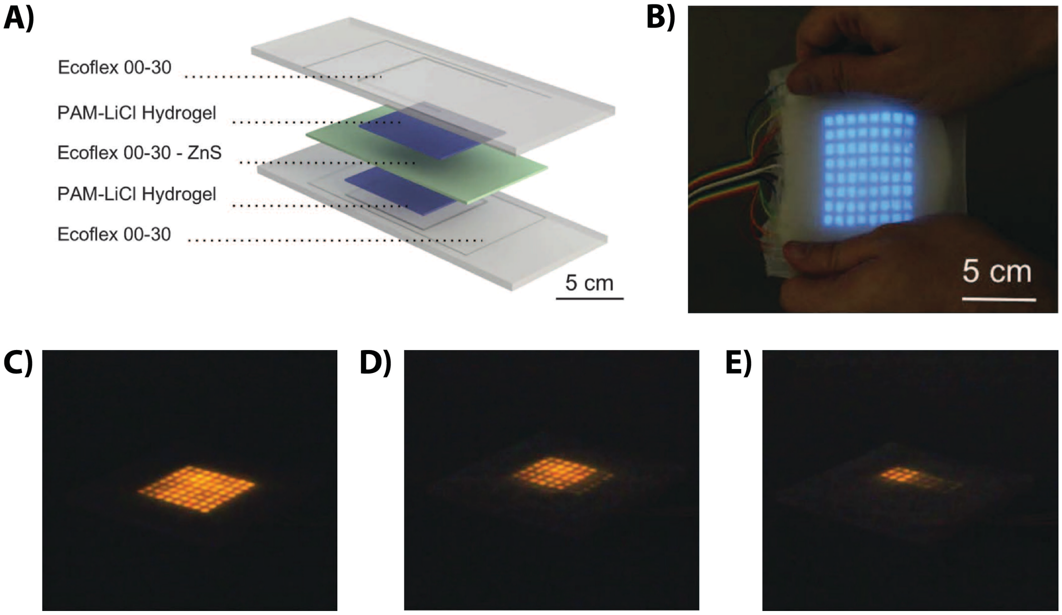

Figure 1.13. Description of a hyperelastic light-emitting capacitor. A) A schematic of the hyperelastic light-emitting capacitor, which consisted of an electroluminescent phosphor-containing layer sandwiched between two ionically-conducting polyacrylamide electrodes and encapsulated in a flexible silicon housing. B) A picture of a multi-pixel display comprised of arrayed capacitors. The display emitted blue light upon application of an electric field (actuation). C) A picture of a multi-pixel display comprised of arrayed capacitors. The entire eight by eight pixel array was actuated and emited orange light. D) A picture of the display from (C), for which a six by six subset of the pixel array was actuated and emitted orange light. E) A picture of the display from C), for which a three by three subset of the pixel array was actuated and emitted orange light. Parts A) – E) were reproduced with permission of The American Association for the Advancement of Science. Copyright 2016.

Larson and coworkers drew inspiration from the architecture of cephalopod skin and investigated soft multi-pixel electroluminescent display-like sheets.[38] Thus, the authors first designed and fabricated hyperelastic light-emitting capacitors, which consisted of a phosphor-containing layer sandwiched between two ionically-conducting polyacrylamide electrodes and encapsulated within a silicon housing (Figure 1.13A). Subsequently, the authors used replica molding to fabricate sheets containing arrays of such devices (Figure 1.13B, Figure 1.13C). For these arrays, the emission of light was induced through the selective application of alternating current electric fields to independent pixels in distinct areas, enabling control over the sheets' patterning and appearance. As an example, Figure 1.13C, Figure 1.13D, and Figure 1.13E show sheets for which eight by eight, six by six, and three by three arrayed pixel subsets have been actuated, respectively. Here, the use of different phosphors in the electroluminescent layers made it straightforward to fabricate devices with distinct colorations; Figure 1.13B and Figure 1.13C show different sheets from phosphors that emit blue and orange light, respectively. These experiments constituted an exciting example of soft devices that possessed spatiotemporally patternable coloration and appeared amenable to integration with more advanced systems.

Yu and coworkers also drew inspiration from the hierarchical multilayer architecture of cephalopod skin and studied the properties of multiplexed optoelectronic systems.[39] The authors therefore designed multilayer unit cells, for which an exploded view schematic is illustrated in Figure 1.14A and corresponding optical images are shown in Figure 1.14B-E. These unit cells consisted of a thermochromic color-changing dye embedded in a polymer matrix, in analogy to a chromatophore (Figure 1.14B); a thin silver layer as a bright white background, in analogy to a leucophore (Figure 1.14C); a silicon diode heating element as an actuator, in analogy to the chromatophores' muscle fibers (Figure 1.14D); and a silicon photodiode as a light sensor, in analogy to photoresponsive opsin-containing functional units (Figure 1.14E). The authors fabricated multilayer, multiplexed arrays comprised of the unit cells on flexible polymeric support substrates; an exploded view schematic of the arrays is illustrated in Figure 1.14F, and a corresponding optical image is shown in Figure 1.14G.

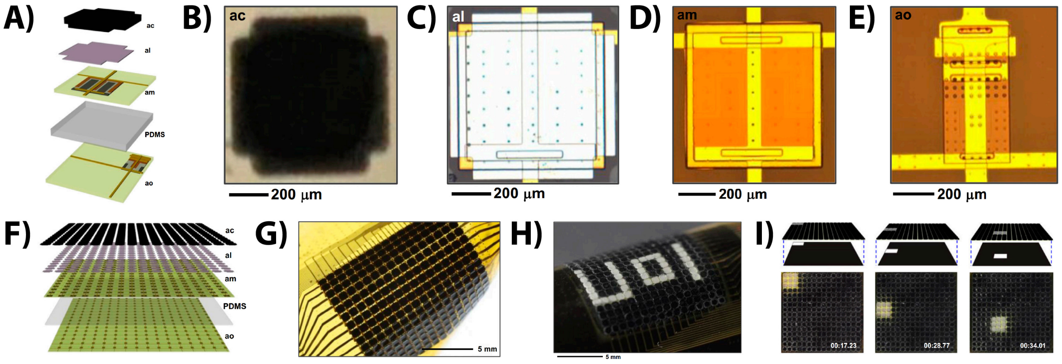

Figure 1.14. Description of flexible, thermoresponsive multiplexed array. A) A schematic of a multilayer unit cell that incorporated essential design features found in cephalopod skin. The unit cells consisted of a thermochromic color-changing dye embedded in a polymer matrix, in analogy to a chromatophore; a thin silver layer as a bright white background, in analogy to a leucophore; a silicon diode heating element as an actuator, in analogy to the chromatophores' muscle fibers; and a silicon photodiode as a light sensor, in analogy to photoresponsive opsin-containing functional units. B) An optical image of a thermochromic equivalent to a chromatophore. C) An optical image of the silver layer and the silicon diode. D) An optical image of the diode. E) An optical image of a photodiode and an associated blocking diode for multiplexing. F) An illustration of an interconnected unit cell array in a complete artificial adaptive camouflage skin. G) An optical image of an interconnected unit cell array in a complete artificial adaptive camouflage skin. H) An image of a bent device that was actuated to display the text "UoI." I) Schematics and corresponding optical images of devices illuminated with light, which stimulated the photodiodes and induced a coloration change from black to white. As a shadow mask moved the light to different locations, the artificial camouflage skins were able to independently adapt their pattern to match the constantly changing position of the incident light. Parts A) – I) were reproduced with permission of the National Academy of Sciences, USA. Copyright 2014.

Through controlled localized heating of the thermochromic color-changing elements, the final integrated systems were capable of producing arbitrary black and white patterns. As an example, Figure 1.14H shows an array that has been programmed to display the text “UoI.” Notably, such arrays maintained their functionality even under mechanical deformation and possessed angle-independent coloration. Furthermore, the authors demonstrated that the integrated systems were able to autonomously sense exogenous stimuli, i.e. incident light, and appropriately adapt their appearance, i.e. change coloration. For instance, Figure 1.14I shows an array that was illuminated with light in different areas – the stimulus was detected by the photodiodes and transduced into localized color changes (from black to white) via heating of specific elements. Overall, these experiments represented a key innovative step forward for multiplexed systems that exhibit fully autonomous operation.

1.3.2 Shape and Texture Modulation

Cephalopods’ flexible and deformable skin allows these animals to contort their body and appendages into seemingly arbitrary geometries and positions.[22,24] As one example, Figure 1.15A shows a common octopus attempting to grab a piece of bait in a glass tube.[24] To reach the bait, the octopus elongates an outstretched arm by a factor of two or more, demonstrating the intrinsic stretchability of its skin.[24] As another example, Figure 1.15B shows a picture of a common octopus’ eye and the surrounding smooth skin.[22] To match its surroundings, the octopus extends small rounded protuberances known as papillae, causing the skin to appear textured.[22] Such mechanical properties make cephalopod skin unique in the animal kingdom and highly attractive as a prototype for systems with reconfigurable shapes and textures.

Rossiter and coworkers drew inspiration from multiple types of cephalopod skin cells and investigated “inverted” artificial chromatophore/iridophore variants.[35] The authors therefore fabricated devices consisting of a dielectric elastomer layer sandwiched by annular carbon grease electrodes and overlaid with a blue-colored gel in the region lacking electrodes (Figure 1.16). In the absence of an applied electric field, the gel-covered central area possessed a specific size/thickness and color intensity, and the surrounding electrode surface was relatively smooth (Figure 1.16A, left and Figure 1.16B, left). However, in the presence of an applied electric field, the central region changed its size/thickness

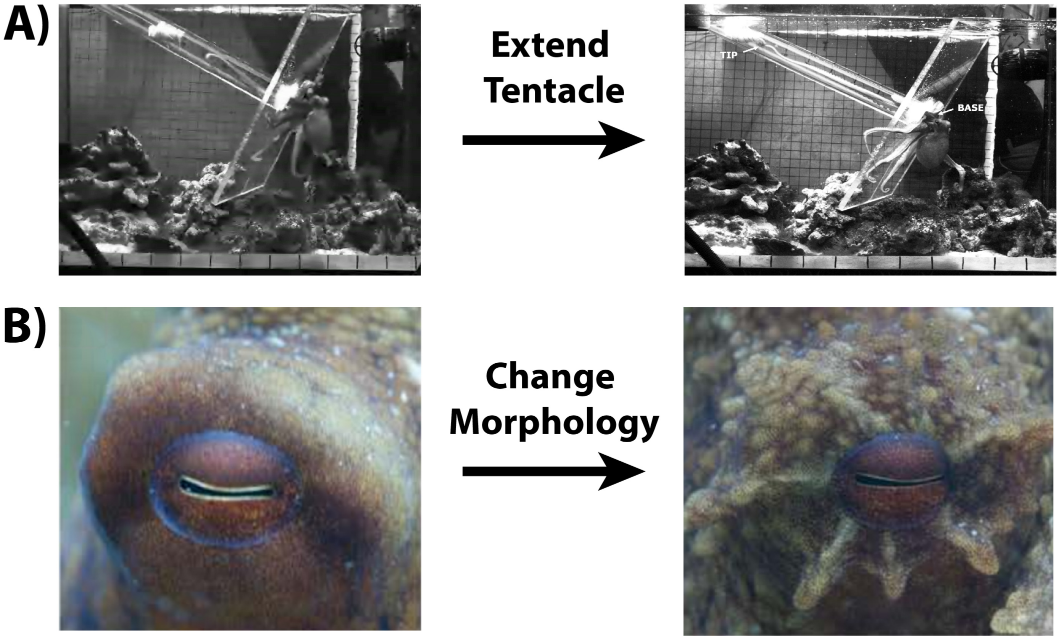

Figure 1.15. Image of an octopus extending its tentacle and of an octopus expanding the papillae around its eye. A) A picture of an octopus and bait positioned at opposite ends of a glass tube, with the animal reaching for the bait (left). After the bait is moved further away, the octopus attempts to reach the bait by extending its arm to twice the original length (right). B) A picture of an octopus with flat skin around its eye (left). The octopus extends papillae to texture the skin (right). Part A) was reproduced with permission of Elsevier. Copyright 2013. Part B) was reproduced with permission of WILEY PERIODICALS, INC. Copyright 2013.

and corresponding color intensity, and the surrounding electrode displayed radial buckling or wrinkling (Figure 1.16A, right and Figure 1.16B, right). These experiments represented an early proof-of-principle demonstration of the simultaneous modulation of the macroscopic texture and color for cephalopod-inspired devices.

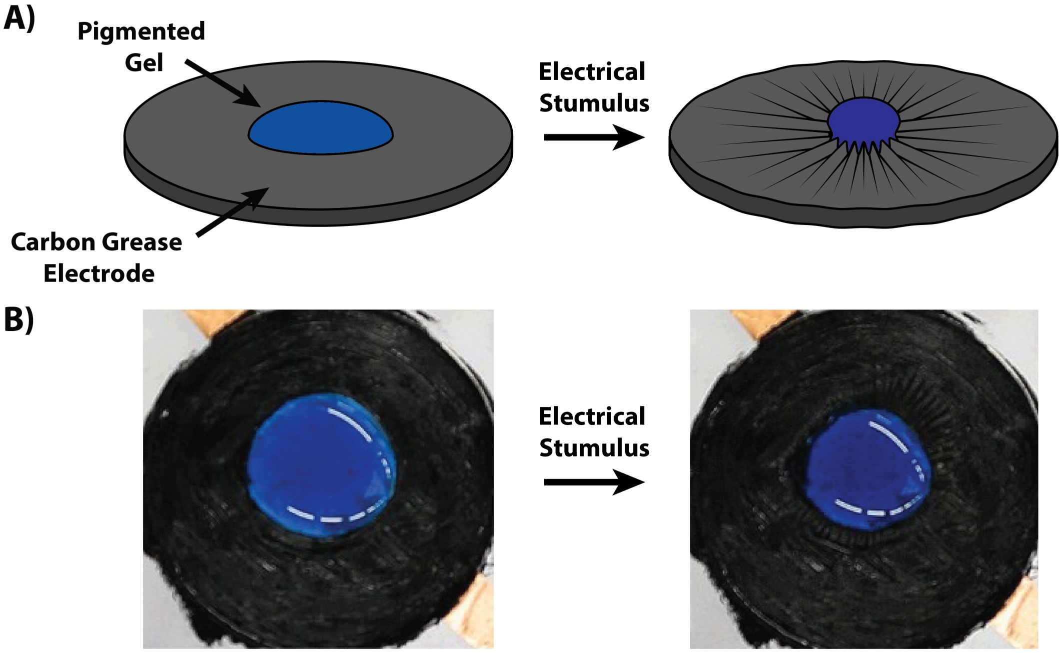

Figure 1.16. Description of an inverted, artificial chromatophore. A) A schematic of an "inverted" artificial chromatophore, which consisted of a central region overlaid with a blue-colored gel layer and surrounded by an annular electrode (left). The application of an electric field induced a change in the geometry and color intensity of the central region, as well as radial buckling/wrinkling of the surrounding electrode's surface (right). B) An image of an "inverted" artificial chromatophore before (left) and after (right) electrical actuation. The device displayed a change in geometry and color intensity, as well as radial buckling/wrinkling of the central region of the surrounding electrode upon application of an electric field. Part B) was reproduced with permission of IOP Publishing. Copyright 2012.

Wang and coworkers drew inspiration from the general optomechanical properties of cephalopod skin and used electromechanochemically-responsive elastomers in electrically-actuated systems with advanced microscale patterning capabilities.[34] For this purpose, the authors designed and fabricated multilayer

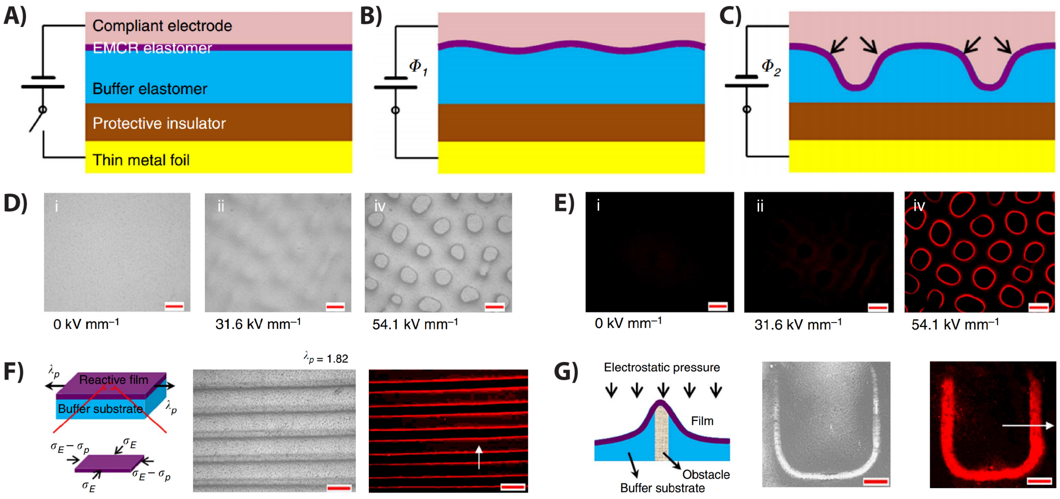

Figure 1.17. Description of an electromechanochemically responsive material. A) A schematic of the electromechanochemically responsive structure, which consisted of a thin metal foil, a rigid protective insulator, a buffer elastomer layer, an electromechanochemically responsive elastomer layer, and a conductive salt solution electrode. B) A schematic of the structure from A), wherein the application of electric fields above material-specific critical values led to the formation of wrinkles. C) A schematic of the system from A), wherein the application of even larger electric fields led to the formation of craters. D) Optical microscope images of an initially flat elastomer layer for which applied electric fields of increasing magnitude induced surface texturing (the formation of craters). E) Fluorescence microscope images of the layer from D) showing that deformation around the crater edges locally converted the spiropyrans to fluorescent merocyanines. F) A schematic of a prestretched electromechanochemically responsive elastomer film (left). An optical microscope image of a prestretched film for which an electric field induced the formation of trenches (middle). A fluorescence microscopy image of the prestretched film demonstrating that the edges of the trenches were fluorescent (right). G) A schematic of an electromechanochemically responsive elastomer film with an obstacle embedded in the underlying buffer substrate (left). An optical microscope image of the film for which an electric field induced deformation along the contour of the obstacle (middle). A fluorescence microscopy image of the deformed film, which demonstrated that the edges of the obstacle were fluorescent (right). Parts A) – G) were reproduced with permission of Macmillan Publishers Ltd: Nature Communications. Copyright 2014.

structures, which consisted of a thin metal foil, a rigid protective insulator, a buffer elastomer layer, an electromechanochemically responsive elastomer layer, and a conductive salt solution electrode (Figure 1.17). In the absence of applied electric fields, the surfaces of such devices were flat, but upon application of electric fields above material-specific critical values, the surfaces became unstable and formed patterns of micrometer-size wrinkles (Figure 1.17B). For even larger applied electric fields, the valleys between the wrinkles were pressed down, forming craters (Figure 1.17C).

As an example, Figure 1.17D shows an optical image of an initially flat electromechanochemically responsive elastomer layer for which an applied electric field had triggered the formation of a pattern of craters (note that the surface recovered its flat state once the stimulus was removed). Notably, the authors demonstrated that larger electric fields induced more substantial deformation around the crater edges and an associated local activation of fluorescence for the spiropyran mechanophores, leading to controllable changes in the effective coloration of the device (Figure 1.17E). Furthermore, the authors showed that prestretching the electromechanochemically responsive elastomer films produced patterns of trenches (Figure 1.17F) and that embedding objects within the buffer layer reproduced their underlying U-shaped topographies on the surface (Figure 1.17G). Altogether, these experiments demonstrated a strategy for the localized rational programming and patterning of microscopic texture and color for cephalopod-inspired devices.

Larson and coworkers drew inspiration from the general malleability of octopus skin and investigated the functionality of their display-like sheets under substantial deformation.[38] Here, the authors employed both single- and multi-pixel variants of their hyperelastic light-emitting capacitors. As one example, Figure 1.18A shows a single-pixel capacitor in its initial and stretched states; the device continued operating under tension, with a predictable increase in the intensity of the emitted light. As another example, Figure 1.18B, Figure 1.18C, and Figure 1.18D shows multi-pixel display-like sheets that were wrapped around a finger, bent, or rolled, respectively. Such patterned analogues of the stretchable devices maintained their normal functionality, i.e. light emission, even when subjected to different types of mechanical deformation. Notably, deformation did not appear to affect localized patterning of the devices' coloration via selective regional application of electric fields (Figure 1.18E). These experiments demonstrated the modulation of both global shape and appearance with independent orthogonal stimuli for cephalopod-inspired devices

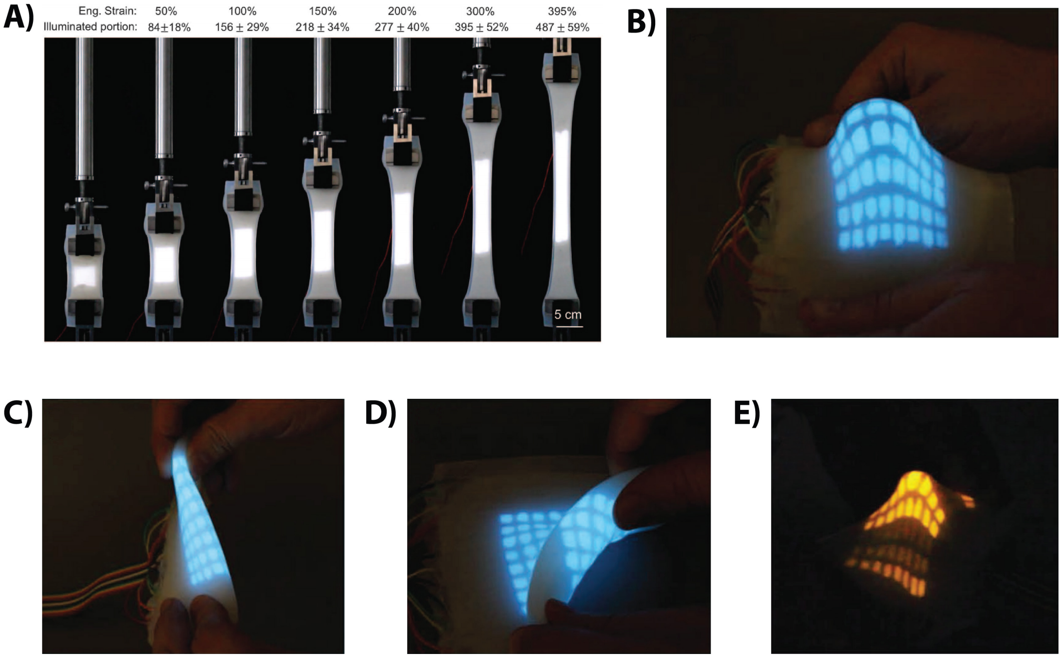

Figure 1.18. Description of a hyperelastic light-emitting capacitor. A) Optical images of a hyperelastic light-emitting capacitor under different applied engineering strains. As the device was stretched to approximately five times its original length (left to right), the functionality was maintained, and the intensity increases in predictable fashion. B) A multi-pixel blue light-emitting display that was deformed by wrapping around a finger. C) A multi-pixel blue light-emitting display that was deformed by folding. D) A multi-pixel blue light-emitting display that was deformed by rolling. E) A deformed multi-pixel orange light-emitting display for which a subset of its pixels was actuated. Parts A) – E) were reproduced with permission of The American Association for the Advancement of Science. Copyright 2016.

1.4 Conclusions

In summary, we have provided an overview of the remarkable abilities of cephalopods and the development of color- and shape-changing materials, devices, and systems directly inspired by these animals. We have highlighted several selected case studies related to switchable coloration, hierarchical multiplexing/pixelation, and shape/texture modulation. These studies constitute substantial progress towards advanced adaptive camouflage and shapeshifting technologies that emulate the abilities of cephalopods. Moving forward, we believe that the integration of cephalopod-inspired materials, devices, and systems with textiles and fabrics represents the natural future progression of research in this field, with such work enabling the development of clothing that functions like a second skin and has a disruptive effect on daily life.

When considering the possibilities afforded by futuristic wearable adaptive camouflage, military applications readily come to mind. Indeed, the US military has invested heavily in the development of advanced fabrics for concealing soldiers from detection by enemy combatants.[40-42] These efforts have often viewed universal camouflage fatigues that function with equal efficacy in any environment as the ultimate lofty goal.[40-42] The utility of such clothing becomes apparent when considering a soldier who travels needs a uniform with a flat surface and large light brown or beige patterning. Subsequently, for optimum concealment in the forest, the soldier needs a uniform with a textured brush-like surface and smaller green and dark brown patterning. Fatigues that adapt to disguise the soldier in both environments therefore may greatly enhance his survivability. This type of game-changing technology could prove invaluable in many combat situations and help to save countless lives.

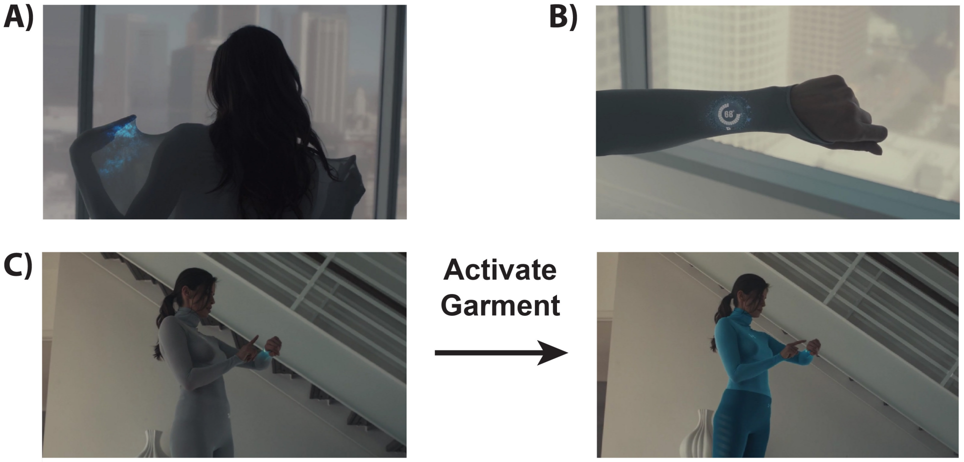

Figure 1.19. Description of a proposed, adaptive garment. A) A picture of Under Armour's "Future Girl," who is in the process of donning a garment that adapts its size and shape to conform to the body of the wearer. B) A picture of the adaptive garment's wrist-mounted control and monitoring panel. C) The panel can actuate the garment and change its coloration from gray (left) to blue (right). Parts A) – C) were reproduced with permission from Under Armour.

Wearable color- and shape-changing technologies also appear highly attractive for leisure applications. Indeed, apparel companies have envisioned customizable fabrics that selectively adapt to the needs of the wearer.[43,44] As an example, Figure 1.19 shows images from an advertisement produced by Under Armour, which is entitled "Future Girl."[43] In this advertisement, a woman dons an advanced garment that dynamically regulates its properties, readily changing shape and size to conform to the user's body (Figure 1.19A). Moreover, the garment contains an integrated control and monitoring panel (Figure 1.19B), allowing the user to modulate the garment's style and coloration at the push of a button for any conceivable activity (Figure 1.19C). Such futuristic clothing presents seemingly endless possibilities, including regulation of an individual's personal thermal comfort and direct continuous monitoring of vital signs. This type of technology could ultimately have a transformative impact on the daily activities of the average person.

The illustrative examples above are just two of a myriad of possibilities, and one can envision many other applications, including (but certainly not limited to) physical therapy for injuries, assistance for the elderly, and support suits for construction crews. However, for wearable cephalopod-inspired adaptive systems to reach their full potential, many scientific and technological challenges must still be overcome by interdisciplinary groups of scientists. For instance, despite the exciting progress made to date, further work and research is certainly necessary within the realms of switchable coloration and hierarchical multiplexing/pixelation. In addition, cephalopod-inspired materials that simultaneously change shape and color are not yet comparable to the state-of-the-art in thematically related fields, such as shape memory polymers and alloys,[45-47] as relatively fewer cephalopod-inspired studies have leveraged concepts from these entrenched areas.[48,49] Moreover, switching speed, power consumption, long-term durability, textile integration, manufacturability, and cost are all significant concerns, which we have not adequately addressed in our discussion. Finally, the envisioned applications inherently necessitate the development of advanced portable control systems for the transduction of sensory inputs from the surroundings into physical effects; such control systems require a degree of complexity comparable to that of the cephalopods' central nervous system, which is a daunting prospect. Although the above numerous remaining challenges are formidable, we hope that the prospect of bringing to life concepts from fables and science fiction, i.e. adaptive camouflage and shapeshifting, will provide an impetus for additional research effort and ensure continued impressive scientific breakthroughs in the described emerging area.

1.5 References

1. Naso, P. O. Metamorphoses; Harvard University Press: Cambridge, 1916; translated by F. J. Miller.
2. von Kaysersberg, J. G. Die Emeis: Dis ist das buch von der Omeissen, und auch Herr der könnig ich diente gern; Johann Grüninger: Strasbourg, 1517.
3. Mallory, M. X-Men: The Characters and Their Universe, 1st ed.; Hugh Lauter Levin Associates: Fairfield, 2006.
4. X-Men: Days of Future Past; 20th Century Fox: Los Angeles, CA, U.S.A., 2014. Film.
5. Maẗhger, L.M.;Denton,E.J.;Marshall,N.J.;Hanlon,R.T. Mechanisms and Behavioural Functions of Structural Coloration in Cephalopods. J. R. Soc., Interface 2009, 6, S149−S163.
6. Hanlon, R. T.; Messenger, J. B. Cephalopod Behavior; Cambridge University Press: Cambridge, England, 1998.
7. Hanlon. R. T.; Chiao, C.-C. C.; Mäthger, L. M.; Buresch, K. C.; Barbosa, A.; Allen, J. J.; Siemann, L.; Chubb. C. Rapid adaptive camouflage in cephalopods. In Animal Camouflage: Mechanisms and Function; Stevens, M., Merilaita, S., Eds.; Cambridge University Press: Cambridge, England, 2011; pp 145–163.
8. Kaufmann, G. director, producer, writer; Orlt, C. producer. Cuttlefish: The Brainy Bunch Television Broadcast. Kings of Camouflage, July 13, 2011. Public Broadcasting Service (PBS).

9. Kreit, E.; Mäthger, L. M.; Hanlon, R. T.; Dennis, P. B.; Naik, R. R.; Forsythe, E.; Heikenfeld, J. Biological Versus Electronic Adaptive Coloration: How Can One Inform the Other? J. R. Soc. Interface 2013, 10, 20120601.
10. Hanlon, R. T. Cephalopod Dynamic Camouflage. Curr. Biol. 2007, 17, R400–R404.
11. Steenfeldt, H. Amazing Squid Changing Color Video File. YouTube, August 13, 2012. https://www.youtube.com/watch?v=OauXCp8l3QI (accessed March 21, 2016).
12. DeMartini, D. G.; Ghoshal, A.; Pandolfi, E.; Weaver, A. T.; Baum, M.; Morse, D. E. Dynamic Biophotonics: Female Squid Exhibit Sexually Dimorphic Tunable Leucophores and Iridocytes. J. Exp. Biol. 2013, 216, 3733–3741.
13. Mäthger, L. M.; Senft, S. L.; Gao, M.; Karaveli, S.; Bell, G. R. R.; Zia, R.; Kuzirian, A. M.; Dennis, P. B.; Crookes-Goodson, W. J.; Naik, R. R.; Kattawar, G. W.; Hanlon, R. T. Bright White Scattering from Protein Spheres in Color Changing, Flexible Cuttlefish Skin. Adv. Funct. Mater. 2013, 23, 3980–3989.
14. DeMartini, D. G.; Krogstad, D. V.; Morse, D. E. Membrane Invaginations Facilitate Reversible Water Flux Driving Tunable Iridescence in a Dynamic Biophotonic System. Proc. Natl. Acad. Sci. USA 2013, 110, 2552–2556.
15. DeMartini, D. G.; Izumi, M.; Weaver, A. T.; Pandolfi, E.; Morse, D. E. Structures, Organization, and Function of Reflectin Proteins in Dynamically Tunable Reflective Cells. J. Biol. Chem. 2015, 290, 15238–15249.

16. Messenger, J. B. Cephalopod Chromatophores: Neurobiology and Natural History. Biol. Rev. 2001, 76, 473–528.

17. Deravi, L. F.; Magyar, A. P.; Sheehy, S. P.; Bell, G. R. R.; Mäthger, L. M.; Senft, S. L.; Wardill, T. J.; Lane, W. S.; Kuzirian, A. M.; Hanlon, R. T.; Hu, E. L.; Parker, K. K. The Structure-Function Relationships of a Natural Nanoscale Photonic Device in Cuttlefish Chromatophores. J. R. Soc. Interface 2014, 11, 20130942.

18. Mäthger, L. M.; Hanlon, R. T. Malleable Skin Coloration in Cephalopods: Selective Reflectance, Transmission and Absorbance of Light by Chromatophores and Iridophores. Cell Tissue Res. 2007, 329, 179–186.

19. Cloney, R. A.; Brocco, S. L. Chromatophore Organs, Reflector Cells, Iridocytes and Leucophores in Cephalopods. Amer. Zool. 1983, 23, 581–592.

20. Wardill, T. J.; Gonzalez-Bellido, P. T.; Crook, R. J.; Hanlon, R. T. Neural Control of Tuneable Skin Iridescence in Squid. Proc. R. Soc. B 2012, 279, 4243–4252.

21. Allen, J. J.; Bell, G. R. R.; Kuzirian, A. M.; Hanlon, R. T. Cuttlefish Skin Papilla Morphology Suggests a Muscular Hydrostatic Function for Rapid Changeability. J. Morphol. 2013, 274, 645–656.

22. Allen, J. J.; Bell, G. R. R.; Kuzirian, A. M.; Velankar, S. S.; Hanlon, R. T. Comparative Morphology of Changeable Skin Papillae in Octopus and Cuttlefish. J. Morphol. 2014, 275, 371–390.

23. Allen, J. J.; Mäthger, L. M.; Barbosa, A.; Hanlon, R. T. Cuttlefish Use Visual Cues to Control Three-Dimensional Skin Papillae for Camouflage. J. Comp. Physiol. A 2009, 195, 547–555.
24. Mazzolai, B.; Margheri, L.; Dario, P.; Laschi, C. Measurements of Octopus Arm Elongation: Evidence of Differences by Body Size and Gender. J. Exp. Mar. Biol. Ecol. 2013, 447, 160–164.
25. Vukusic, P.; Sambles, J. R. Photonic Structures in Biology. Nature 2003, 424, 852–855.
26. Kinoshita, S.; Yoshioka, S. Structural Colors in Biological Systems: Principles and Applications; Osaka University Press: Osaka, 2005.
27. Kinoshita, S. Structural Colors in the Realm of Nature; World Scientific Publishing Co.: Singapore, 2008.
28. Saito, A. Material Design and Structural Color Inspired by Biomimetic Approach. Sci. Technol. Adv. Mater. 2011, 12, 064709.
29. Wu, L.; He, J.; Shang, W.; Deng, T.; Gu, J.; Su, H.; Liu, Q.; Zhang, W.; Zhang, D. Optical Functional Materials Inspired by Biology. Adv. Opt. Mater. 2016, 4, 195–224.
30. Fu, Y.; Tippets, C. A.; Donev, E. U.; Lopez, R. Structural Colors: from Natural to Artificial Systems. WIREs Nanomed. Nanobiotechnol. Online early access. DOI: 10.1002/wnan.1396. Published Online: Mar 8, 2016. http://onlinelibrary.wiley.com/doi/10.1002/wnan.1396/pdf (accessed June 15, 2016).

31. Kramer, R. M.; Crookes-Goodson, W. J.; Naik, R. R. The Self-Organizing Properties of Squid Reflectin Protein. Nat. Mater. 2007, 6, 533–538.
32. Phan, L.; Walkup, W. G., IV; Ordinario, D. D.; Karshalev, E.; Jocson, J.-M.; Burke, A. M.; Gorodetsky, A. A. Reconfigurable Infrared Camouflage Coatings from a Cephalopod Protein. Adv. Mater. 2013, 25, 5621–5625.
33. Phan, L.; Ordinario D. D.; Karshalev, E.; Walkup IV, W. G.; Shenk, M. A.; Gorodetsky, A. A. Infrared Invisibility Stickers Inspired by Cephalopods. J. Mater. Chem. C 2015, 3, 6493–6498.
34. Wang, Q.; Gossweiler, G. R.; Craig, S. L.; Zhao, X. Cephalopod-Inspired Design of Electro-Mechano-Chemically Responsive Elastomers for On-Demand Fluorescent Patterning. Nat. Commun. 2014, 5, 4899.
35. Rossiter, J.; Yap, B.; Conn, A. Biomimetic Chromatophores for Camouflage and Soft Active Surfaces. Bioinspir. Biomim. 2012, 7, 036009.
36. Rossiter, J.; Conn, A.; Cerruto, A.; Winters, A.; Roke, C. Colour Gamuts in Polychromatic Dielectric Elastomer Artificial Chromatophores. Proc. SPIE 2014, 9056, 905620/1–905620/8.
37. Morin, S. A.; Shepherd, R. F.; Kwok, S. W.; Stokes, A. A.; Nemiroski, A.; Whitesides, G. M. Camouflage and Display for Soft Machines. Science 2012, 337, 828–832.
38. Larson, C.; Peele, B.; Li, S.; Robinson, S.; Totaro, M.; Beccai, L.; Mazzolai, B.; Shepherd, R. Highly Stretchable Electroluminescent Skin for Optical Signaling and Tactile Sensing. Science 2016, 351, 1071–1074.

39. Yu, C.; Li, Y.; Zhang, X.; Huang, X.; Malyarchuk, V.; Wang, S.; Shi, Y.; Gao, L.; Su, Y.; Zhang, Y.; Xu, H.; Hanlon, R. T.; Huang, Y.; Rogers, J. A. Adaptive Optoelectronic Camouflage Systems with Designs Inspired by Cephalopod Skins. Proc. Natl. Acad. Sci. USA 2014, 111, 12998–13003.
40. Hartcup, G. Camouflage: A History of Concealment and Deception in War; Scribner's: New York, 1980.
41. Cox, M. Congress Pushes Ahead with Plan for Joint Camouflage Uniform, 2014. Military.com. http://www.military.com/daily-news/2014/12/04/congress-pushes-ahead-with-plan-for-joint-camouflage-uniform.html (accessed February 29, 2016).
42. Hambling, D. US Army Calls for Ideas on Invisible Uniforms for Soldiers, 2015. New Scientist. https://www.newscientist.com/article/mg22630202.200-us-army-calls-for-ideas-on-invisible-uniforms-for-soldiers/#.VUsfWNOqpBd (accessed March 26, 2016).
43. Kinghorn, M. Under Armour, "Future Girl" Video File. Vimeo, June 25, 2013. https://vimeo.com/69062155 (Accessed February 20, 2016).
44. Pierce, D. How Under Armour Plans to Turn Your Clothes Into Gadgets, 2016. Wired. http://www.wired.com/2016/01/under-armour-healthbox/ (Accessed Apr 2, 2016).
45. Sun, L.; Huang, W. M.; Ding, Z.; Zhao, Y.; Wang, C. C.; Purnawali, H.; Tang, C. Stimulus-Responsive Shape Memory Materials: A Review. Mater. Design 2012, 33, 577–640.

46. Jani, J. M.; Leary, M.; Subic, A.; Gibson, M. A. A Review of Shape Memory Alloy Research, Applications and Opportunities. Mater. Design 2014, 56, 1078–1113.
47. Hager, M. D.; Bode, S.; Weber, C.; Schubert, U. S. Shape Memory Polymers: Past, Present and Future Developments. Prog. Polym. Sci. 2015, 49, 3–33.
48. Laschi, C.; Cianchetti, M.; Mazzolai, B.; Margheri, L.; Follador, M.; Dario, P. Soft Robot Arm Inspired by the Octopus. Adv. Robot. 2012, 26, 709–727.
49. Chatterjee, S.; Velankar, S. S. Reversibly Texturing Active Surfaces with Spatial and Temporal Control. J. Intell. Mater. Syst. Struct. 2015, 26, 328–339.

CHAPTER 2 Self-Assembly of the Cephalopod Protein Reflectin[‡]

2.1 Abstract

Films from the cephalopod protein reflectin demonstrate multifaceted functionality as infrared camouflage coatings, proton transport media, and substrates for growth of neural stem cells. A detailed study of the in vitro formation, structural characteristics, and stimulus response of such films is presented. The reported observations hold implications for the design and development of advanced cephalopod-inspired functional materials.

2.2 Introduction

Cephalopods (squid, octopuses, and cuttlefish) have captivated the imagination of scientists for more than a century due to their highly sophisticated nervous systems, surprisingly complex behavioral patterns, and visually stunning camouflage displays.[1–6] Due to such unique capabilities and characteristics, these marine invertebrates have emerged as an exciting source of inspiration for the development of novel materials and technologies.[7–15] Within this context, our group has investigated cephalopod structural proteins known as reflectins, which possess an amino acid sequence consisting of characteristic conserved (M/F-D-X_5)(M-D-X_5)$_n$(M-D-$X_{3/4}$) motifs separated by variable linker regions and containing a high percentage of charged and aromatic residues.[16–22] We have discovered that films from the *Doryteuthis (Loligo) pealeii* reflectin A1 (RfA1)

[‡] This chapter appears in the published article of the same title. Naughton, K. L.; Phan, L.; Leung, E. M.; Kautz, R.; Lin, Q.; Van Dyke, Y.; Marmiroli, B.; Sartori, B.; Arvai, A.; Li, S.; Pique, M. E.; Naeim, M.; Kerr, J.P.; Aquino, M. J.; Roberts, V.A.; Getzoff, E.D.; Zhu, C.; Bernstorff, S.; Gorodetsky, A.A. Self-Assembly of the Cephalopod Protein Reflectin, *Adv. Mater.*, **2016,** *28*, 8405–8412.

isoform function as stimuli-responsive reconfigurable infrared camouflage coatings,[23,24] feature electrical properties that rival those of well-known artificial proton conductors,[25,26] and support the proliferation and differentiation of neural stem cells.[27] These findings have indicated that both RfA1 and the extended reflectin protein family hold promise as advanced functional materials.

Despite the technological potential of RfA1, a clear relationship between this protein's higher-order structure/organization in films and in vitro functionality has remained elusive to date. For RfA1, the elucidation of such key structure–function relationships has proven challenging due to the reflectin protein family's propensity for aggregation into variable-size nanoparticles,[17,18,20,22,23] exquisite sensitivity to changes in salt concentration,[17,18,22] apparent lack of significant secondary structure in solution,[17,18,21–23] and unusual amino acid sequence.[16–22] Nonetheless, Morse and co-workers have demonstrated the emergence of ß-sheet character for salt-precipitated RfA1 nanoparticle aggregates[18] and the electrostatically driven cyclable assembly/ disassembly of RfA1 nanoparticles (as a surrogate for phosphorylation-induced condensation of reflectins within photonic ultrastructures in vivo).[21,22] Moreover, complementary theoretical modeling and fluorescence measurements have suggested that RfA1's conserved motifs form amphiphilic domains, for which the hydrophobic regions govern nanoparticle assembly and interactions.[22] However, while the prior work provided important insight, it did not explore the formation and nano-/microstructure of RfA1 films on solid substrates or elucidate structure–function relationships for such films. Consequently, there exists an opportunity for further detailed structural characterization of RfA1-based ensembles, with the goal of better understanding their multifaceted functionality and exciting in vitro properties.

Herein, we present a systematic study of the in vitro formation, structural characteristics, and stimulus response of films from the *D. pealeii* RfA1 isoform. First, we prepare solutions of the RfA1 nanoparticles according to reported protocols[23–27] and assess the relative solvent accessibility of RfA1's characteristic sequence motifs[18,19,21,22] (and intervening variable linker regions) via deuterium exchange mass spectrometry (DXMS).[28–32] Subsequently, we evaluate the geometry and size of RfA1 nanoparticles via small-angle X-ray scattering (SAXS) in solution[33–38] and via scanning electron microscopy (SEM) on solid substrates.[39–42] In turn, we study the self-assembly of the RfA1 nanoparticles into films via in situ grazing-incidence small-angle X-ray scattering (GISAXS)[43–48] and demonstrate that such films feature a distinct nanostructure, which is slightly altered by an exogenous stimulus (water). Finally, we detect the emergence of ß-sheet character in the films with grazing-incidence wide-angle X-ray scattering (GIWAXS).[43–48] Based on our findings, we develop a multi-scale model for the nanostructure of RfA1 films, which indicates that aggregated substrate-confined RfA1 bears some similarities to processed forms of the artificial sulfonated fluoropolymer Nafion, as well as opens new avenues for the rational design of this unique protein's optical and electrical functionality.

2.3 Experiment

2.3.1 Dynamic Light Scattering of Reflectin

We began our studies by preparing and characterizing aqueous solutions of the histidine-tagged *Doryteuthis (Loligo) pealeii* reflectin A1 isoform (RfA1) according to previously reported procedures.[23–27] The size of RfA1 nanoparticles in solution was characterized with dynamic light scattering (DLS) at the UC Irvine Laser Spectroscopy Facility (LSF). For the DLS measurements, solutions of RfA1 with a concentration of 3.6 mg/mL were prepared by dissolving lyophilized, purified reflectin protein in deionized water (Milli-Q) as previously reported.[23,25] The protein solutions were analyzed with a Malvern Zeta-Sizer Nano S instrument.

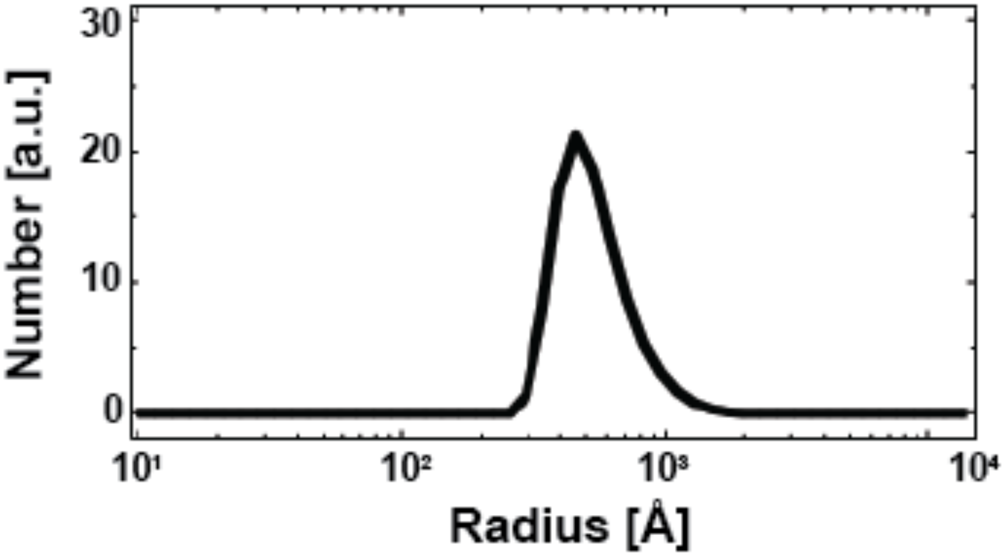

Figure 2.1. DLS Trace of of Reflectin A1 in solution. A representative dynamic light scattering spectrum obtained for a solution of RfA1.

Here, DLS measurements for multiple independently prepared solutions indicated that RfA1 adopted a multimeric state and formed nanoparticles with a peak hydrodynamic radius of $R_H \approx 470\ (\pm 200)$ Å (as illustrated by the spectrum in Figure 2.1). From Gaussian fits of the DLS spectra, we extracted the nanoparticles' polydispersity index (PdI) according to the equation $\mathrm{PdI} = (\sigma/d)^2$, where d is the mean size and σ is the standard deviation of the distribution obtained from the fit.[49–52] The analysis furnished typical indices of ≈0.06 to ≈0.07, thereby indicating the presence of a single reasonably uniform size mode for our solution-borne RfA1 nanoparticles (note that polydisperse samples typically possess PdI values greater than ≈ 0.1).[49–52] We found that the observed unimodal distributions generally resembled the ones previously reported for *D. pealeii* RfA1 solutions by both Tao et al.[18] and Phan et al.,[23] but differed somewhat from the bimodal ones found for *D. opalescens* RfA1 solutions by Levenson et al.[22] The differences likely resulted from variations in pH, ionic strength, protein concentration, and amino acid sequence, which are all known to influence the self-assembly of reflectins.[17,18,20,22,23] In general, the characteristics of our aqueous RfA1 solutions were analogous to those described in the literature.

2.3.2 Deuteron Exchange Mass Spectroscopy of Reflectin

With our solutions in hand, we used DXMS to probe the state of RfA1 in our nanoparticles.[28–32] This technique quantitatively measures the exchange of a protein's backbone amide protons with deuterons upon dilution of the aqueous solvent with deuterium oxide.[28–32] The resulting time-dependent proton/deuteron exchange map furnishes information on the solvent accessibility throughout the protein chain and can therefore indicate the presence of secondary or tertiary structure.[28–31] The solvent accessibility of the RfA1 amino acid residues was evaluated with DXMS at the University of California, San Diego DXMS Proteomics Resource according to protocols adapted from the literature.[32] First, solutions of RfA1 with a concentration of 1 mg/mL were prepared by dissolving the protein in Milli-Q water according to established procedures.[23,25] Next, 9 µL of deuterium oxide was added to 3 µL of a 1 mg/mL RfA1 solution. The exchange of protons with deuterons was allowed to occur for either 10 s or 30 s prior to terminating the reaction through addition of 18 µL of a quench buffer, which contained 1.6 M guanidinium chloride, 0.8 % formic acid, and 16.6 % glycerol. The quenched solution was in turn cooled on ice for 1 min before being frozen on solid CO_2. As comparative controls, non-deuterated and fully deuterated samples were prepared in similar fashion. For the non-deuterated samples, 9 µL of water was added to 3µL of an RfA1 solution at 0˚C, and quenched as above. For the fully deuterated samples, 9µL of 0.5% formic acid in deuterium oxide was added to 3µL of an RfA1 solution, stored overnight at room temperature, and then quenched. Each quenched sample was digested through proteolysis, with the resulting peptide fragments separated on a C18 HPLC column. The eluates were analyzed with an Orbitrap Elite S-2 hybrid mass spectrometer (Thermo Fisher), and the SEQUEST software program (Thermo Fisher) was used to identify the likely sequence of the parent peptide ions, resulting in a set of 238 peptides. The program DEX3[53] was used to analyze the non-deuterated peptides in order to determine those peptides with a good fit to their theoretical isotopic profile, a good signal-to-noise ratio, and no overlap with other signals or contaminants within a mass range that included the deuterated peptide species. The resulting set of 100 unique peptides provided complete coverage of RfA1, except for residues 273-278. The deuterium content of each peptide found for the 10 s, 30 s, and fully deuterated samples was determined with DEX3. The analysis was further verified by the observation of a consistent deuteration level among overlapping peptides. Eighteen of the 100 peptides were found in multiple ionic states; each state was identified and analyzed independently, providing an additional internal consistency check.

Figure 2.2. DXMS exchange map for Reflectin A1. The proton/deuteron exchange map for the RfA1 sequence after 10 s (top) and 30 s (bottom) of exposure to deuterium oxide. The rainbow color code (right) indicates the percent deuteration for each residue, which was calculated as the average over all peptides containing that residue. The black ovals correspond to the six conserved motifs of RfA1, as defined by Morse and co-workers.[18,21]

Figure 2.2 illustrates the exchange maps obtained from a representative DXMS experiment for RfA1 nanoparticles. After 10 s, we found that ≈ 10% more of the amide protons in the linker regions than in the conserved motifs had exchanged for deuterons (Figure 2.2, top), and after 30 s, we found that ≈ 20% more of the amide protons in the linker regions than in the conserved motifs had exchanged for deuterons (Figure 2.2, bottom). Thus, within the large nanoparticles, the RfA1 protein was sufficiently structured to confer greater solvent protection to the conserved motifs (as defined by Morse and co-workers)[18,21] than to the intervening linker regions. Furthermore, the differences in exchange rates among the individual motifs suggested that they occupied distinct surrounding environments. These observations were in general agreement with fluorescence measurements indicating that some tyrosines and tryptophans (which are located in the motifs) are sequestered to hydrophobic environments.[22] Altogether, our DXMS data implied that the conserved sequence motifs were participating in hydrogen bonding interactions and/or were relatively more confined to the interior of RfA1 ensembles.

2.3.3 Small-angle X-Ray Scattering of Reflectin

We proceeded to investigate the geometry of RfA1 nanoparticles with SAXS. In a SAXS experiment, collimated and monochromatic X-rays are scattered by solution-dispersed objects, producing a diffuse 2D pattern (Figure 2.3), part of which is then circularly integrated to generate a 1D analogue.[33–38] The scattering data yields information on the objects' size, shape, conformation, and order over a length scale of ≈10 to ≈10^5 Å.[33–38]

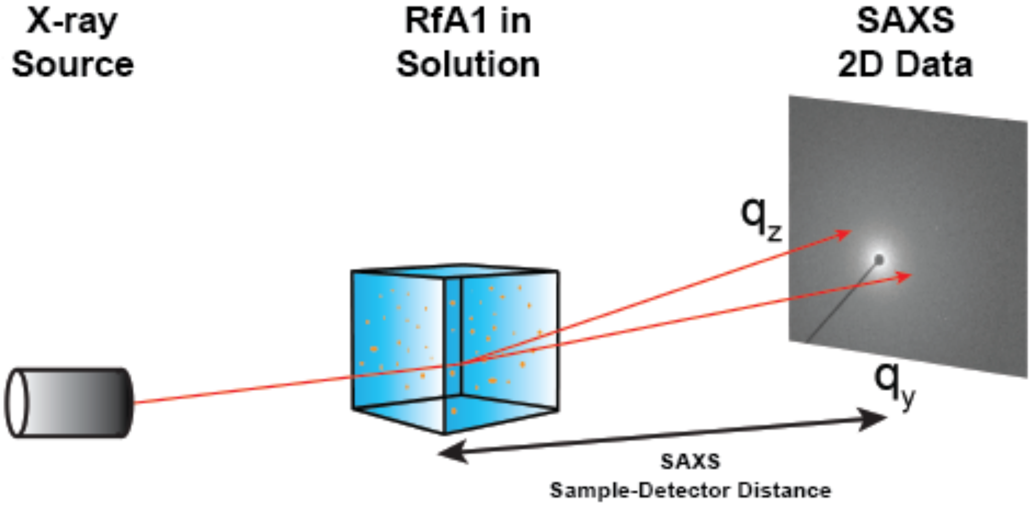

Figure 2.3. Illustration of a typical SAXS experiment. A schematic of a small-angle X-ray scattering experiment for RfA1 in solution. The incident X-rays are scattered by the solution-dispersed macromolecules, yielding a 2D pattern (data for RfA1 is shown).

The SAXS experiments were performed at the 5-ID-D beamline of the DND-CAT synchrotron research center, Advanced Photon Source, Argonne National Laboratory. Radiation with an energy of 12 keV, which corresponds to a wavelength of 1.03 Å, was scattered by the sample, forming a 2-D pattern (see Figure 2.3 for a typical pattern) on a 162 mm CCD X-ray detector (Mar-USA). The collection time was 3 s and the sample to detector distance was 8504 mm. The detector covered the range of $0.0016 < q < 0.091$ Å^{-1}, where the scattering vector $q = (4\pi/\lambda) \sin(\theta)$, λ is the wavelength of the incident X-rays, and 2θ is the scattering angle. The data from the detector was integrated and analyzed with the PRIMUS and IRENA software programs.[54,55]

Figure 2.4 illustrates a plot of the integrated scattering intensity *I*(*q*) versus the scattering vector *q* obtained for a representative solution of RfA1 nanoparticles. To analyze the data, we adopted a unified approach[57–60] and fit the experimental curves with a physically motivated sticky hard sphere model, which accounted for the nanoparticle shape via a spheroidal form factor and for the nanoparticle interactions via a "sticky" structure factor.[61,62] This analysis was motivated by observations that RfA1 forms nanoparticles, which influence one another through a combination of electrostatic and hydrophobic forces.[17,18,20,22,23] Moreover, our approach was precedented by the successful application of similar models to other solution-borne protein nanoparticles, i.e., casein micelles.[63–65] Here, we discovered reasonable agreement between our experimental observations and the simulated scattering intensity profile (Figure 2.4).

To quantify the geometry of our RfA1 nanoparticles, we inspected and analyzed the low-q ($q < 0.003$ Å^{-1}) Guinier and high-q ($q > 0.003$ Å^{-1}) Porod regions of the scattering intensity profile (Figure 2.4 and Figure 2.5A, Figure 2.5B). For the Guinier region, we examined a plot of the integrated scattering intensity $I(q)$ versus the square of the scattering vector q^2 (Figure 2.5A) and used the exponential approximation $I(q) \sim \exp\left(-(R_{G}*q)^2/3\right)$ to extract the radius of gyration R_G, within the context of a unified fit.[57–60] A computational analysis of the simulated scattering profile, yielded an R_G value of ≈ 416 Å (Table 2.1) which was similar to the R_H value obtained via DLS. Interestingly, the R_G to R_H ratio for the nanoparticles was ≈ 0.9, which was greater than the ideal ratio of ≈ 0.78 expected for a homogeneous hard sphere and hinted that our nanoparticles were not symmetric.[66,67] For the Porod region, we examined a plot of the integrated scattering intensity times the fourth power of the scattering vector $I(q)\cdot q^4$ versus the scattering vector q (Figure 2.5B) and used the power law approximation $I(q) \sim q^{-P}$ to extract the exponent P, again within the context of a unified fit.[57–60] A computational analysis of the simulated scattering profile yielded a P of 1.5 (Table 2.1) which was intermediate between the exponent expected for a prolate or needle-like ellipsoid ($P = 1$) and a random coil in a good solvent ($P = 1.67$), indicating an elongated spheroidal object.[34,58–60] In their totality, these calculations revealed the size of our RfA1 nanoparticles and provided insight into their shape in solution.

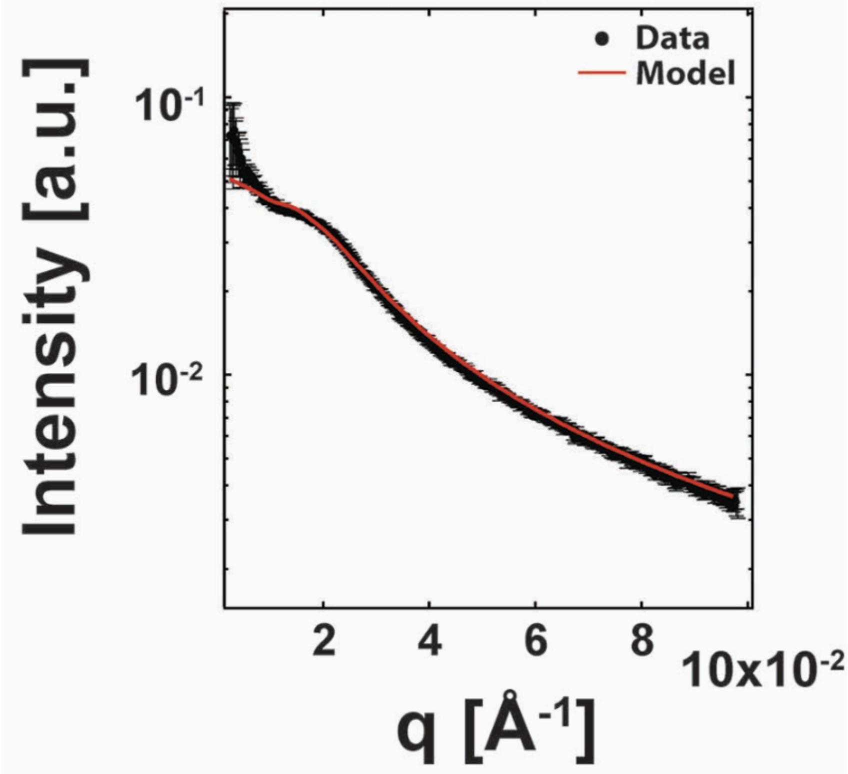

Figure 2.4. Log-lin plot showing data and simulated model fit for a SAXS experiment for solution phase reflectin. A 1D plot of the scattering intensity $I(q)$ versus the scattering vector q obtained for a solution of RfA1. The black circles represent the experimental data, and the red line represents the simulated scattering intensity profile.

We in turn further evaluated our Guinier plot of the integrated scattering intensity *I*(*q*) versus the square of the scattering vector q^2 (Figure 2.5A). The shape of this plot provides insight into the presence (and types) of intermolecular interactions for solution-borne objects; a linear curvature indicates no interactions, a concave upward curvature indicates attraction, and a concave downward curvature indicates repulsion.[33–38,68] Here, we observed a concave upward relationship between *I* and q^2 (Figure 2.5A). This relationship confirmed the presence of interactions between the RfA1 nanoparticles, in agreement with literature reports for electrostatically controlled reflectin nanoparticle assembly[18,22] and our postulated sticky sphere model. We next formulated a Kratky plot of the integrated scattering intensity times the square of the scattering vector $I(q)\cdot q^2$ versus the scattering vector *q* (Figure 2.5C). The shape of this plot provides insight into the spatial spread of objects; a bell-type curve indicates globular behavior and a plateau at large *q* values indicates Gaussian chain-like behavior.[33-38,69] We observed a distinct peak in the Kratky plot, with $I(q)\cdot q^2$ decaying and plateauing at higher *q* (Figure 2.5C). This dependence suggested that the RfA1 nanoparticles possessed flexible regions, but were at least partially compact, in agreement with both DXMS observations of limited solvent accessibility for portions of the protein and our postulated sticky sphere model.

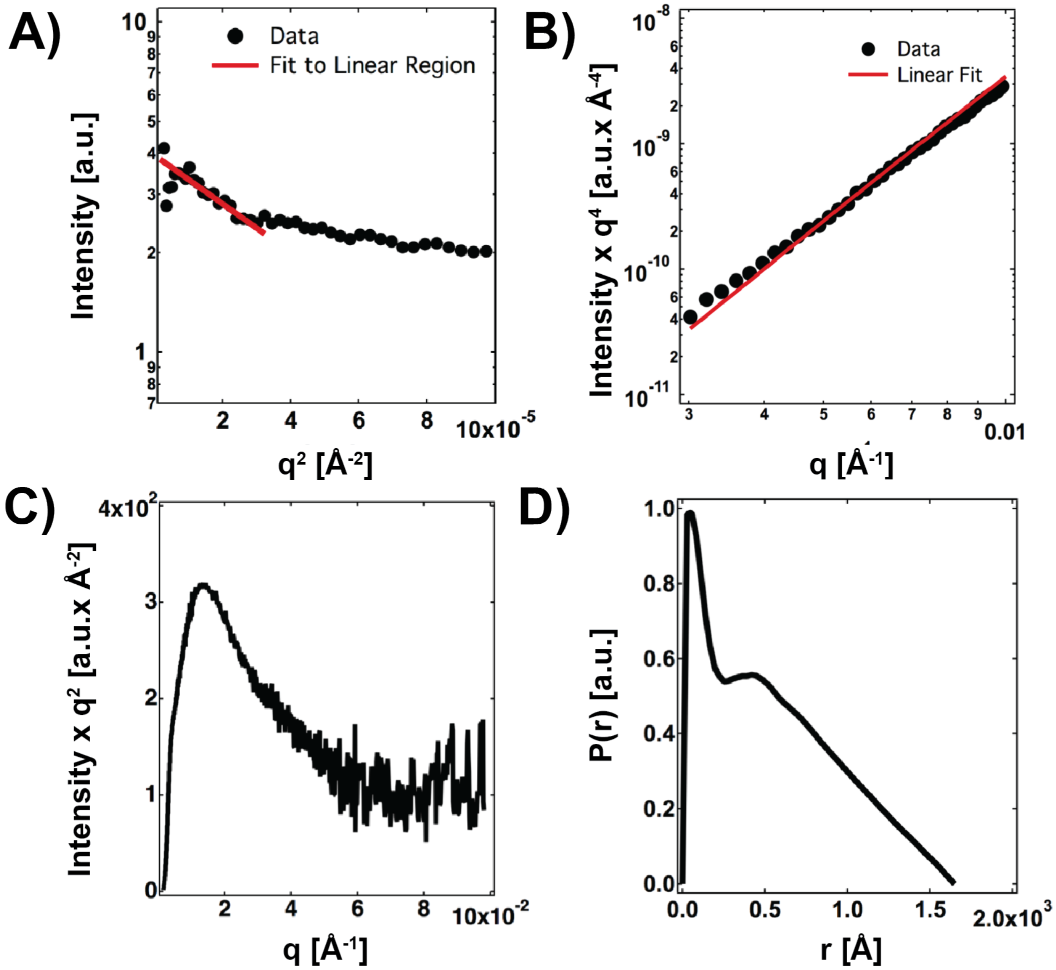

Figure 2.5. Guinier Plot showing a fit to the linear region, a Porod plot showing a fit to the linear region, a Kratky plot, and a distribution function. The plots correspond to the scattering intensity profile in Figure 2.4. A) A Guinier plot of the integrated scattering intensity I(q) versus the square of the scattering vector q^2. The black dots represent the experimental data, and the red line represents a fit of a linear region of the data at low q. **B)** A Porod plot of the integrated scattering intensity times the fourth power of the scattering vector I(q) x q^4 versus the scattering vector q. The black dots represent the experimental data, and the red line represents a linear fit of the data. **C)** A Kratky plot of the integrated scattering intensity times the square of the scattering vector I(q) x q^2 versus the scattering vector q. **D)** A representative plot of the distance distribution P(r) versus the distance r.

We subsequently generated and analyzed the pair-wise distance distribution function for our RfA1 nanoparticles (Figure 2.5D). This function describes the distribution of distances between all points within an object in real space and yields a more intuitive description of its geometry and mass distribution (but does

<table>
<tr><td colspan="3">Equation Used for Simulations of the Scattering Intensity</td></tr>
<tr><td colspan="3">$I(q) = (Ge^{-\frac{q^2 R_G{}^2}{3}} + BI^{-P})\mathrm{S}(\varphi, \mathrm{k}, \tau)$</td></tr>
<tr><td colspan="3">Parameters Obtained from Simulations of the Scattering Intensity</td></tr>
<tr><td>Name</td><td>Definition</td><td>Simulated Value</td></tr>
<tr><td>G [a.u.]</td><td>Guinier coefficient</td><td>1.7×10^{-2}</td></tr>
<tr><td>R_G [Å]</td><td>Radius of gyration</td><td>416</td></tr>
<tr><td>B [a.u.]</td><td>Porod coefficient</td><td>3.3×10^{-5}</td></tr>
<tr><td>P [a.u.]</td><td>Power law slope</td><td>1.5</td></tr>
<tr><td>φ [a.u.]</td><td>Volume fraction</td><td>0.01</td></tr>
<tr><td>k [a.u.]</td><td>Perturbation factor</td><td>0.1</td></tr>
<tr><td>τ [a.u.]</td><td>Stickiness</td><td>0.5</td></tr>
</table>

Table 2.1 A table stating the equation and listing the values used to develop a simulated SAXS profile. The equation and corresponding parameters employed to generate the simulated scattering curve in **Figure 2.4**. The equation and parameter definitions were adapted from the protocols in reference 56.

not directly represent the polydispersity for a solution of such objects).[33–38,70] A representative plot of the distance distribution *P*(*r*) versus the distance *r* featured an irregular shape, two main peaks at $r \approx 60$Å and $r \approx 420$ Å, and a maximum dimension of $D_{\max} \approx 1650$ Å (Figure 2.5C). The shape and presence of multiple peaks were consistent with expectations for interacting elongated particles or asymmetric multi-domain objects,[34,71,72] and the *r* value of ≈ 420 Å was similar to the radii extracted from the DLS and SAXS measurements. Moreover, the maximum possible dimension of approximately three to four times the measured radii was compatible with the notion that the nanoparticles form multimers (presumably dimers), although the precise relative orientation of the nanoparticles was difficult to define with absolute certainty.[34,71,72] Altogether, this analysis provided additional nuanced insight into the geometry and interactions of our RfA1 nanoparticles.

2.3.4 Scanning Electron Microscopy of Reflectin

To obtain additional independent validation for our interpretation of the SAXS data, we investigated substrate-bound RfA1 nanoparticles with SEM.[39–42] In an SEM experiment, a beam of incident electrons is scanned over a sample, furnishing information on the samples' morphology and com- position.[39–42] This technique enables the evaluation of both nanoscale and microscale features, even for delicate biological materials.[39–42]

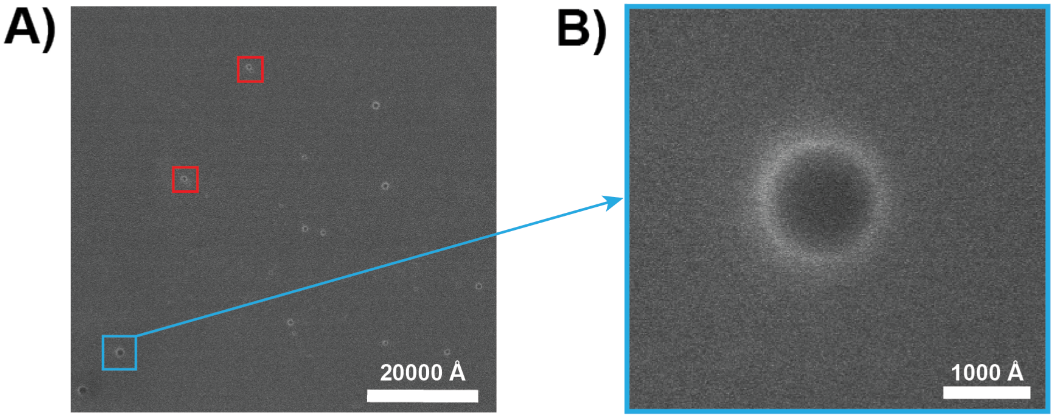

Figure 2.6. Scanning electron microscopy characterization of substrate bound reflectin nanoparticles A) A representative scanning electron microscopy images of RfA1 nanoparticles on a silica substrate. The red squares indicate RfA1 nanoparticle multimers (dimers). The blue square indicates an individual RfA1 nanoparticle that was imaged at increased magnification. B) A close- up high-resolution scanning electron microscopy image of the RfA1 nano- particle enclosed by the blue square in (A).

The SEM characterization was performed at the UC Irvine Materials Research Institute (IMRI). The RfA1-modified silica substrates used for imaging were attached to an aluminum specimen mount (Ted Pella) with conductive silver paint (Ted Pella). These substrates were then coated with a ~ 0.5 nm thick iridium layer, which was deposited with an IBS/e sputter coater (South Bay Technology). Subsequently, the samples were imaged with a Quanta 3D SEM (FEI) outfitted with an Everhart Thornley detector at an accelerating voltage of 5-10 kV. The highest resolution images were obtained under high vacuum (8×10^{-5} mbar). The images were processed and analyzed with the FIJI software program.[73] Note that the calculations of the average radii from the SEM images excluded nanoparticles which were difficult to unambiguously distinguish from the background or which featured uncertain sizes due to overlap with one another.

Figure 2.6A shows a representative image of RfA1 nanoparticles that have been cast from solution onto a silica substrate, and Figure 2.6B shows a close-up high-resolution image of a single nanoparticle. An analysis of the particles in Figure 2.6A yielded an average radius of ≈ 450 (±160) Å, in agreement with both the R_H and R_G values extracted from the DLS and SAXS measurements, respectively. Interestingly, the RfA1 nanoparticles appeared to deviate slightly from a perfectly spherical shape, supporting our analysis of the scattering intensity profile (note that sample preparation and substrate interactions likely influence the shape as well). Furthermore, the nanoparticles were not necessarily isolated and formed multimers (dimers) in some instances (Figure 2.6A, red squares), corroborating our interpretation of the Guinier plot and pair-wise distance distribution function. In their totality, these and our other observations definitively confirmed that the RfA1 nanoparticles resembled asymmetric and interacting spheroids.

2.3.5 Grazing-incidence small-angle X-ray scattering of Reflectin

Having evaluated the geometry of both solution-borne and substrate-bound RfA1 nanoparticles, we studied the formation, nanostructure, and stimulus response of RfA1 films with GISAXS.[43–48] In a GISAXS experiment, collimated and monochromatic X-rays are scattered by the surface of a film near its critical angle, producing a 2D pattern (Figure 2.7), for which a horizontal segment can be integrated to generate a 1D analogue.[43–48] Given that GISAXS probes the same length scale as small-angle X-ray scattering and possesses the surface sensitivity of grazing incidence X-ray diffraction, the technique is well suited for elucidating the size, shape, interactions, and distribution of objects within even poorly ordered films.[43–48] Furthermore, *in situ* GISAXS experiments make it possible to monitor the emergence of structure during film formation and to follow the evolution of structure in response to exogenous stimuli.[43,44,47] The GISAXS measurements were conducted at the SAXS beamline at Elettra-Sincrotrone

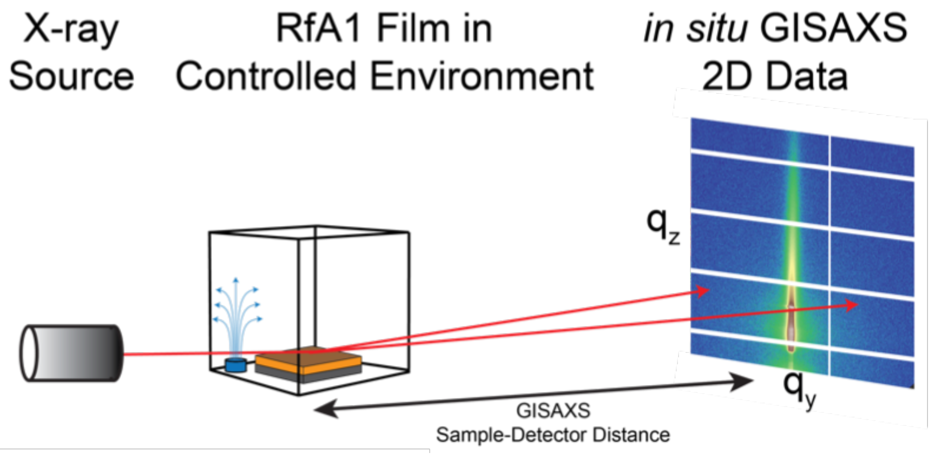

Figure 2.7. Illustrated description a typical in situ GISAXS experiment. A) A schematic of a grazing incidence small angle X-ray scattering experiment for an RfA1 film. The incident X-rays are scattered by substrate-confined aggregated macromolecules, yielding a 2D pattern (data for RfA1 is shown).

Trieste, Italy.[74] Radiation with an energy of 8 keV, which corresponds to a wavelength of $\lambda = 1.55$ Å, was scattered by the sample, forming a 2-D pattern (see Figure 4A for a typical image) on a Pilatus 1M detector with a pixel size of 172 μm × 172 μm (Dectris). The collection time was between 1 s and 4 s, the sample to detector distance was 3010 mm (as determined with a silver behenate calibration sample), and the grazing incidence angle was 0.10°. The detector covered the range of $0.002 < q < 0.12$ Å^{-1}, where the scattering vector $q = (4\pi/\lambda) \sin(\theta)$, λ is the wavelength of the incident X-rays, and 2θ is the scattering angle. For in situ experiments, the measurements were performed in a closed chamber with constant monitoring of the relative humidity by a hygrometer. The data from the detector was integrated with the NIKA software program (the q_z integration range for Figure 2.8 and Figure 2.9 in the main text was 0.041 Å^{-1} to 0.045 Å^{-1}) and analyzed with the IRENA software program.[55,75].

Figure 2.8 illustrates a plot of the integrated scattering intensity $I_G(q)$ versus the horizontal scattering vector q_y obtained at various times during the self-assembly/formation of a representative RfA1 film (as induced by evaporation of aqueous solvent from a concentrated RfA1 nanoparticle solution drop-cast directly onto a silica substrate). To analyze the data, we adopted a unified approach and t our curves with a sticky hard sphere model,[61,62] with the goal of capturing the geometry and order of nanoparticles within the interior of the RfA1 films. This analysis was motivated by our direct observations of interacting RfA1 nanoparticles via SAXS and SEM. Furthermore, our approach was precedented by the successful application of similar models for understanding the behavior of interacting casein micelles in thin films.[65,76–78] Here, we again discovered reasonable agreement between the experimental observations and simulated scattering intensity profiles (Figure 2.8).

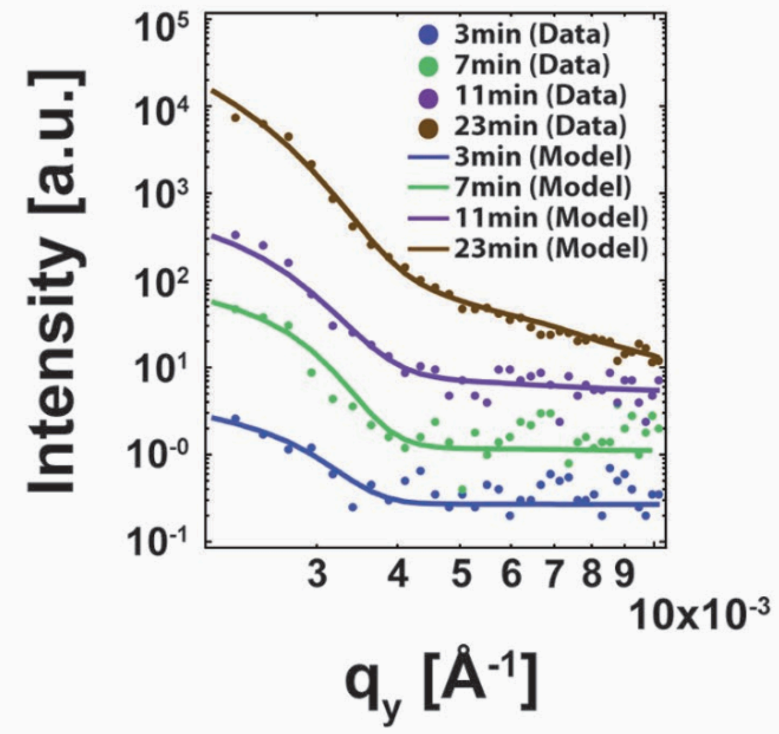

Figure 2.8. Plot showing experimental data and simulated scattering profiles from an in situ GISAXS experiment of reflectin self-assembly. A 1D plot of the grazing incidence small- angle X-ray scattering intensity $I_G(q)$ versus the scattering vector q_Y obtained at different times during the self-assembly/formation of a film from RfA1 nanoparticles. The measurements were obtained at 3 (blue), 7 (green), 11 (purple), and 23 (brown) min after initiation of assembly. The circles represent the experimental data, and the lines represent the simulated scattering intensity profiles. The green, purple, and brown curves have been offset vertically for clarity.

To understand the emergence of structure during RfA1 film formation, we monitored changes in the effective RfA1 nanoparticle geometry by extracting the radius of gyration R_G and exponent P from the scattering profiles collected at different time points after initiation of film assembly (Figure 2.8 and Table 2.2). First, at $t = 3$ min (corresponding to an experiment on a nearly aqueous system), we calculated an R_G of 830 Å, which was approximately twice the radius obtained in solution, and an exponent P of 1.5, which was consistent with the notion of an elongated spheroidal object.[34,58–60] The increase in R_G indicated that most of our nanoparticles likely adopted a multimeric (dimeric) state, presumably due to a greater local concentration as solvent rapidly evaporated from the surface. Next, at t = 7 min, we observed a slight increase in the nanoparticle radius to an R_G of 840 Å but no change in their shape, with a P of 1.5. Subsequently, at t = 11 min, we found an additional increase in the nanoparticle radius to an R_G of 880 Å and a change in the exponent to a P of 1.7, which was similar to the value expected for a random coil in a good solvent (P = 1.67).[34,58–60] The altered geometry implied that the nanoparticle interior had become more solvent accessible, potentially due to interactions with the substrate. Finally, at t = 23 min (corresponding to complete loss of solvent), we found a nanoparticle radius R_G of 910 Å and an exponent P of 2.1, which was similar to the value expected for an oblate or plate-like ellipsoid (P = 2).[34,58–60] The final geometry suggested that the nanoparticles had become flattened upon moving from solution to the interior of a substrate-bound film. Such substantial geometric changes probably resulted from a combination of factors, including the absence of solvation, presence of both lateral and vertical confinement, enhanced interparticle interactions due to crowding, and proximity-induced merger between neighbors (note that the effect of any single contribution cannot be readily deconvoluted). Altogether, our observations and analysis provided mechanistic insight into the formation and nanostructure of RfA1 films.

<table>
<tr><td colspan="6">Equation Used for Simulations of the Scattering Intensity</td></tr>
<tr><td colspan="6">$I(q) = (Ge^{-\frac{q^2 {R_G}^2}{3}} + BI^{-P})\mathrm{S}(\varphi, \mathrm{k}, \tau)$</td></tr>
<tr><td colspan="6">Parameters Obtained from Simulations of the Scattering Intensity</td></tr>
<tr><td>Parameter</td><td>Explanation</td><td>Simulated Value t = 3 min</td><td>Simulated Value t = 7 min</td><td>Simulated Value t = 11 min</td><td>Simulated Value t = 23 min</td></tr>
<tr><td>G [a.u.]</td><td>Guinier coefficient</td><td>0.1</td><td>2.0</td><td>1.4</td><td>174</td></tr>
<tr><td>R_G [Å]</td><td>Radius of gyration</td><td>830</td><td>840</td><td>880</td><td>910</td></tr>
<tr><td>B [a.u.]</td><td>Porod coefficient</td><td>1.0×10^{-8}</td><td>1.0×10^{-7}</td><td>1.7×10^{-7}</td><td>8.4×10^{-7}</td></tr>
<tr><td>P [a.u.]</td><td>Power law slope</td><td>1.5</td><td>1.5</td><td>1.7</td><td>2.1</td></tr>
<tr><td>φ [a.u.]</td><td>Volume fraction</td><td>0.16</td><td>0.16</td><td>0.08</td><td>0.01</td></tr>
<tr><td>k [a.u.]</td><td>Perturbation factor</td><td>0.1</td><td>0.1</td><td>0.1</td><td>0.1</td></tr>
<tr><td>τ [a.u.]</td><td>Stickiness</td><td>12</td><td>10</td><td>4.9</td><td>0.1</td></tr>
</table>

Table 2.2 A table stating the equation and listing the values used to develop a simulated GISAXS profile for a reflectin self-assembly experiment. The equation and corresponding parameters employed to generate the simulated scattering curves in **Figure 2.8**. The equation and parameter definitions were adapted from the protocols in reference 56.

We subsequently evaluated the effect of an exogenous stimulus on the nanostructure of our RfA1 films, again with in situ GISAXS.[43,44,47] We specifically focused our efforts on the con- sequences of hydration (water uptake), which is a prerequisite for protonic conductivity in RfA1 films and has been shown to change the films' volume/thickness (and reflectance).[23,25] Figure 2.9 illustrates the experimental and simulated scattering intensity profiles obtained for a representative RfA1 film both before and after hydration, with water uptake induced by an increase in relative humidity. Before hydration (relative humidity of < 50%), we extracted a nanoparticle radius R_G of 920 Å and an exponent P of 2.0 from the simulated scattering profiles (Table 2.3). This measurement indicated the RfA1 films were comprised of large oblate ellipsoids, in agreement with our observations during film formation.

After hydration (relative humidity of we extracted a nanoparticle radius R_G of 890 Å and an exponent P of 1.8 from the simulated scattering profiles

(Table 2.3). This measurement indicated that the ellipticity of our nanoparticles had decreased, in agreement with expectations for their transition from a dry (solid state-like) to a solvated (more solution phase-like) environment. In their totality, our measurements revealed the nanostructure governing the functionality of the RfA1 films in their hydrated state.

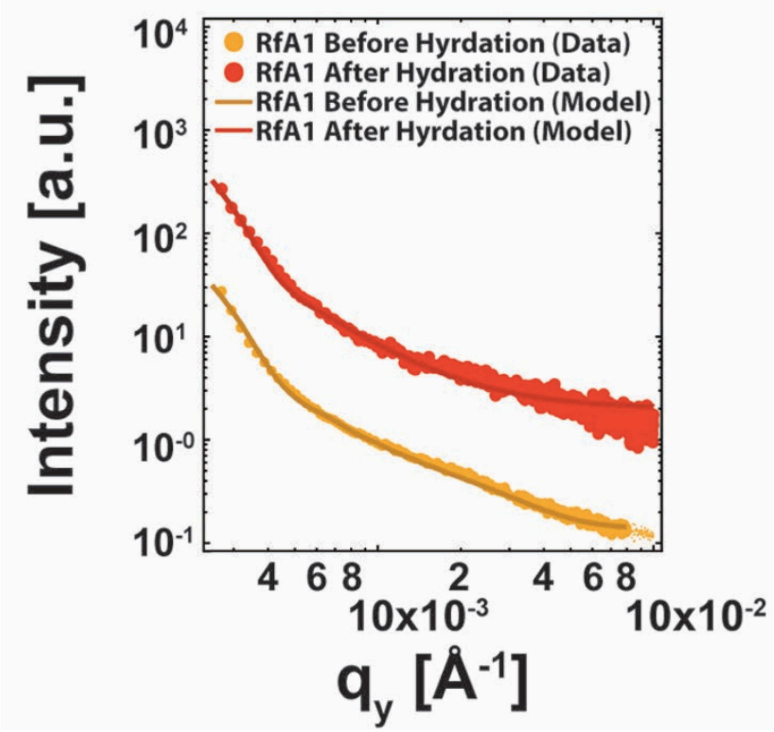

Figure 2.9. A 1D plot of the grazing incidence small-angle X-ray scattering intensity $I_G(q)$ versus the scattering vector q_y obtained for an RfA1 film before and after hydration. The orange circles represent the experimental data obtained before hydration, and the solid orange line represents the simulated scattering intensity profile. The red circles represent the experimental data obtained after hydration, and the solid red line represents the simulated scattering intensity profile. The orange curve has been offset vertically for clarity.

<table>
<tr><th colspan="4">Equation Used for Simulations of the Scattering Intensity</th></tr>
<tr><td colspan="4">$I(q) = (Ge^{-\frac{q^2 R_G{}^2}{3}} + BI^{-P})S(\varphi, \mathrm{k}, \tau)$</td></tr>
<tr><td colspan="4">Parameters Obtained from Simulations of the Scattering Intensity</td></tr>
<tr><td>Name</td><td>Definition</td><td>Simulated Value Before Hydration</td><td>Simulated Value After Hydration</td></tr>
<tr><td>G [a.u.]</td><td>Guinier coefficient</td><td>191</td><td>17.7</td></tr>
<tr><td>R_G [Å]</td><td>Radius of gyration</td><td>920</td><td>890</td></tr>
<tr><td>B [a.u.]</td><td>Porod coefficient</td><td>5.5×10^{-5}</td><td>1.5×10^{-5}</td></tr>
<tr><td>P [a.u.]</td><td>Power law slope</td><td>2.0</td><td>1.8</td></tr>
<tr><td>φ [a.u.]</td><td>Volume fraction</td><td>0.01</td><td>0.01</td></tr>
<tr><td>k [a.u.]</td><td>Perturbation factor</td><td>0.10</td><td>0.10</td></tr>
<tr><td>τ [a.u.]</td><td>Stickiness</td><td>0.10</td><td>0.10</td></tr>
</table>

Table 2.3 A table stating the equation and listing the values used to develop a simulated GISAXS profile to model geometrical changes of a reflectin film upon stimulus. The equation and corresponding parameters employed to generate the simulated scattering curves in Figure 2.9. The equation and parameter definitions were adapted from the protocols in reference 56.

2.3.6 Grazing-incidence wide-angle X-ray scattering of Reflectin

Finally, we probed the presence of secondary structure in our RfA1 films with GIWAXS, which is a surface sensitive variant of wide-angle X-ray scattering (WAXS).[43–48] In a GIWAXS experiment, collimated and monochromatic X-rays are scattered by the surface of a film, producing a 2D pattern (Figure 2.10), part of which is then circularly integrated to generate a 1D analogue.[43–48] WAXS and GIWAXS probe length scales of ≈ 1 Å to ≈ 10 Å that are relevant to atomic and molecular distances.[43–48] For protein ensembles, WAXS furnishes distinct signatures for random coils, α-helices, and β-sheets (although the degree/ strength of any specific secondary structure cannot be readily extracted).[79–82]

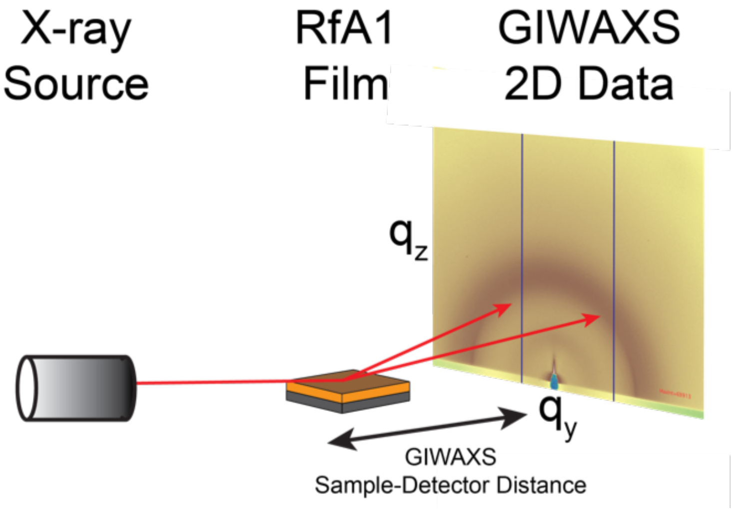

Figure 2.10. A schematic of a grazing incidence wide-angle X-ray scattering experiment for an RfA1 film. The incident X-rays are scattered by substrate-confined aggregated macromolecules, yielding a 2D pattern (the data for RfA1 are shown).

The GIWAXS experiments were performed at the 7.3.3 beamline of the Advanced Light Source at the Lawrence Berkeley National Laboratory. Radiation with an energy of 10 keV, which corresponds to a wavelength of 1.24 Å was scattered by the film, forming a 2- D pattern on a Pilatus 2M detector (Dectris). The collection time was 5 s, the sample to detector distance was 276 mm, and the grazing incidence angle was 0.10°. The detector covered the range of $0.07 < q < 4.17$ Å^{-1}, where the scattering vector $q = (4\pi/\lambda) \sin(\theta)$, λ is the wavelength of the incident X-rays, and 2θ is the scattering angle. The measurements were performed in the absence of hydration because background scattering precluded reliable data collection and analysis at high relative humidities. The data from the detector was

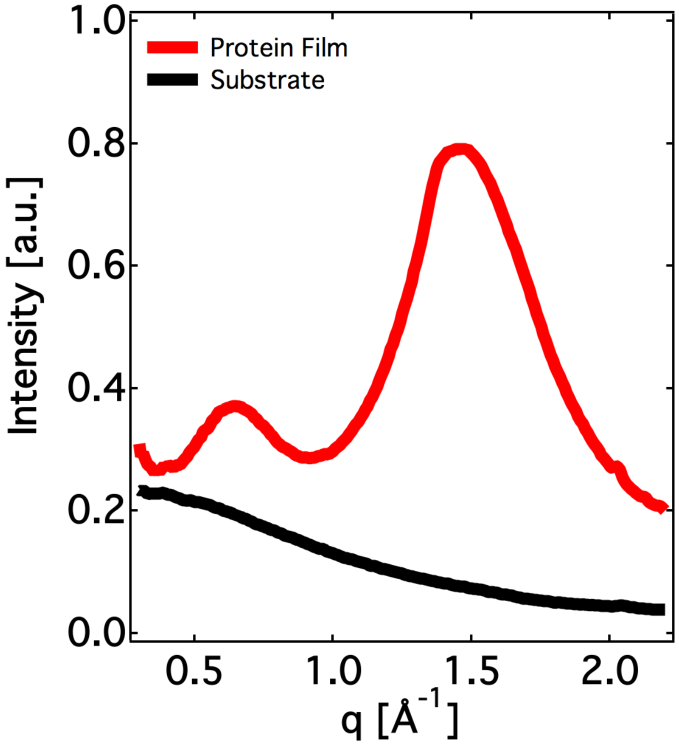

Figure 2.11. A 1D plot of the grazing incidence wide-angle X-ray scattering intensity $I_W(q)$ versus the scattering vector q obtained for a RfA1 film and for a blank silicon dioxide substrate. Note the absence of any obvious peaks in the trace corresponding to the silicon dioxide substrate. The measurement was performed under conditions identical to those used for collection of the data in **Figure 2.11**.

integrated with the NIKA software program and analyzed with the IRENA software program. [55,74] Figure 2.11 illustrates a plot of the integrated scattering intensity $I_W(q)$ versus the scattering vector q obtained for a representative RfA1 film in the absence of hydration. This plot displayed two clear peaks at $q \approx 0.63$ Å^{-1} and $q \approx 1.41$ Å^{-1} (note that identical spectra collected for blank substrates did not reveal any obvious signals). The observed peaks corresponded to distances of ≈ 4.5 Å and ≈ 10 Å and matched the characteristic interstrand and intersheet separations found for β-sheets.[79,81] Such profiles are well-known "fingerprints" of β-sheet character for proteins,[79,81] and similar signatures have been observed with WAXS for salt-precipitated RfA1 nanoparticles.[18] Given our DXMS measurements and the reported theoretical calculation of hydrophobic moments for RfA1,[22] the observed secondary structure can be directly linked to RfA1's conserved sequence motifs and may emerge from enhanced inter-particle interactions and/or protein folding within the confined interior of the RfA1 films. Overall, our measurements and analysis provided an initial step toward forging a connection between the atomic- level structure and in vitro functionality of RfA1 ensembles.

2.4 Results

Based on an analysis of our data and findings, we propose a model for the formation and nanostructure of RfA1 films, as illustrated in Figure 2.12. When dispersed in solution, RfA1 forms asymmetric prolate (elongated) nanoparticles, which transiently interact with one another, presumably via flexible regions through a combination of electrostatic and hydrophobic forces. During film self-assembly on solid substrates, the nanoparticles aggregate or cluster together, with an accompanying evolution of their geometry to oblate (flattened). The particles thus endow the RfA1 films with an internal nanostructure, which is slightly altered under conditions relevant to the films' functionality (high relative humidities). Furthermore, RfA1 displays β-sheet character in its aggregated state, which can be associated with the protein's conserved motifs (and likely holds relevance for its functionality/self-assembly properties). Overall, this general model furnishes a detailed overview of the hierarchical organization of RfA1 ensembles both in solution and the solid state.

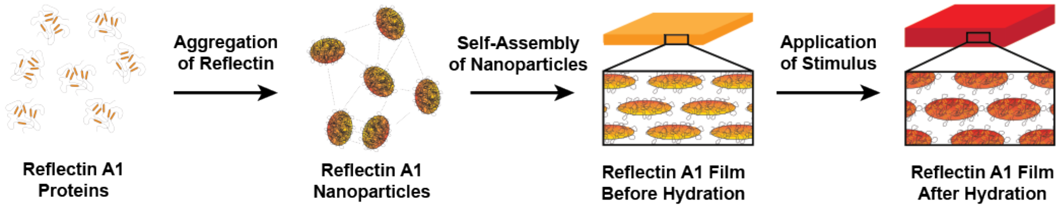

Figure 2.12. Illustration of the hierarchical organization of RfA1 in solution and in films. When dispersed in solution, RfA1 aggregates into interacting nanoparticles with an asymmetric prolate (elongated) geometry. When self-assembled into films, the RfA1 nanoparticles still interact and adopt an oblate (flattened) geometry, which changes slightly upon the application of a stimulus (an increase in relative humidity leading to hydration).

Our observations are significant from the perspective of the in vitro dynamic optical properties of RfA1 films.[17,20,23] We have shown that such films function as reconfigurable infrared camouflage coatings, for which the reflectance can be tuned from the visible to the near infrared with an acidic vapor stimulus (note that BSA controls do not display such functionality).[23] We rationalized our previous findings by suggesting that the RfA1 coatings were nanostructured, with acid-induced changes in electrostatic repulsion among the constituent nanoparticles (presumably through protonation of RfA1) accounting for the coatings' swelling and the accompanying shifts in reflectance.[23] Here, the discovery that RfA1 films possess a stimuli-responsive nanostructure, together with the recent demonstration that pH changes dictate electrostatic interactions among solution-borne RfA1 nanoparticles,[22] provide support for this prior postulate. Importantly, based on our findings, we envision controlling the interactions among solution-borne (and substrate-confined) nanoparticles via site-directed mutagenesis and fabricating RfA1 films that feature highly specific optical responses to variable exogenous stimuli. Consequently, our work establishes a connection between the structure and optical functionality of RfA1 films in vitro and may constitute a conceptual foundation for the rational development of programmable RfA1-based adaptive optics.

Our observations are also significant from the perspective of the in vitro electrical properties of RfA1 films.[25,26] We have shown that bulk RfA1 is an excellent proton conductor, with figures of merit rivaling those reported for many artificial state-of-the-art proton-conducting materials.[25] We explained our previous findings by postulating that RfA1 films likely possess an internal structure and that they may be segregated into distinct hydrophobic and proton-conducting hydrophilic regions (with the latter likely serving as efficacious conduits for proton transport).[25] Here, our X-ray scattering experiments confirm that the RfA1 films are nanostructured. Moreover, our DXMS measurements, together with recent fluorescence studies and theoretical modeling of hydrophobic moments for RfA1,[22] indicate that RfA1 ensembles are indeed segregated into distinct hydrophobic (solvent-protected) and hydrophilic (solvent-exposed) regions. This type of segregated nanostructure resembles the one reported for proton-conducting membranes from the sulfonated fluoropolymer Nafion,[83] suggesting that aggregated reflectin may constitute a biological analogue of this material. Importantly, based on our findings, we envision controlling the size of the nanoparticles in solution and in turn forming films with distinct nanostructures that are optimized for proton conduction. Consequently, our work establishes a relationship between the structure and electrical functionality of RfA1 films in vitro and may open opportunities for rationally "evolving" RfA1 (and other reflectins) for improved performance in protonic devices.

Finally, our findings merit consideration within the context of reflectins' key role in the dynamic adaptive coloration capabilities of cephalopods. Indeed, these proteins are components of various optically active ultrastructures found in cephalopod skin, including membrane-bound spherical microparticles in leucophores,[84,85] layered stacks of membrane-enclosed platelets in iridophores,[21,86] and muscle fiber-ringed networks of pigment granules in chromatophores.[87,88] However, refectins have stubbornly resisted atomic-level structural characterization, exhibiting little-to-no organized secondary or tertiary structure in solution.[16–23] Our measurements indicate that RfA1's conserved sequence motifs serve a structural/organizational function and directly implicate the motifs in the emergence of β-sheet secondary structure for RfA1 ensembles, which are analogous to the protein's aggregated and crowded state in vivo. Given the high sequence identity among the known reflectin isoforms,[16–22] we postulate that our findings may hold relevance for better understanding these proteins' role and function as part of larger ultrastructures.

2.5 Conclusion

In summary, we have developed a detailed understanding of the in vitro formation, nanostructure, and stimulus response of functional films from *D. pealeii* reflectin A1 isoform. The aggregated state of the protein was interrogated with DLS, DXMS, and SAXS in solution, as well as with SEM, GISAXS, and GIWAXS at solid substrates. Our experiments indicate that the protein self-assembles into a specific arrangement at the nanoscale, enabling us to develop a model for the organization of RfA1 films, as well as suggest strategies for enhancing their properties. Altogether, our findings shed insight into the relationship between the structure and function of reflectins in general and hold implications for the design and development of advanced cephalopod-inspired materials.

2.6 References

1. Abbott, N. J., Williamson, R., Maddock, L., Eds. *Cephalopod Neurobiology: Neuroscience Studies in Squid, Octopus, and Cuttlefish;* Oxford University Press: Oxford, 1995.
2. Borrelli, L; Fiorito, G. In *Learning and Memory: A Comprehensive Reference*; Byrne, J.H., Ed.; Academic Press: Oxford, 2008; Vol. 1, pp 605–627.
3. Maẗhger, L. M.; Denton, E. J.; Marshall, N. J.; Hanlon, R. T. Mechanisms and Behavioural Functions of Structural Coloration in Cephalopods. J. R. Soc., Interface 2009, 6, S149−S163.
4. Hanlon, R. T.; Messenger, J. B. Cephalopod Behavior; Cambridge University Press: Cambridge, England, 1998.
5. Hanlon. R. T.; Chiao, C.-C. C.; Mäthger, L. M.; Buresch, K. C.; Barbosa, A.; Allen, J. J.; Siemann, L.; Chubb. C. Rapid adaptive camouflage in cephalopods. In Animal Camouflage: Mechanisms and Function; Stevens, M., Merilaita, S., Eds.; Cambridge University Press: Cambridge, England, 2011; pp 145–163.
6. Kaufmann, G. director, producer, writer; Orlt, C. producer. Cuttlefish: The Brainy Bunch Television Broadcast. Kings of Camouflage, July 13, 2011. Public Broadcasting Service (PBS).

7. Kreit, E.; Mäthger, L. M.; Hanlon, R. T.; Dennis, P. B.; Naik, R. R.; Forsythe, E.; Heikenfeld, J. Biological Versus Electronic Adaptive Coloration: How Can One Inform the Other? J. R. Soc. Interface 2013, 10, 20120601.
8. Rolandi, M. R. Rolandi, R. Self-assembled Chitin Nanofibers and Applications. *Adv. Colloid Interface Sci*. **2014**, *207*, 216–222.
9. Yu, C.; Li, Y.; Zhang, X.; Huang, X.; Malyarchuk, V.; Wang, S.; Shi, Y.; Gao, L.; Su, Y.; Zhang, Y.; Xu, H.; Hanlon, R. T.; Huang, Y.; Rogers, J. A. Adaptive Optoelectronic Camouflage Systems with Designs Inspired by Cephalopod Skins. Proc. Natl. Acad. Sci. USA 2014, 111, 12998–13003.
10. Wang, Q.; Gossweiler, G. R.; Craig, S. L.; Zhao, X. Cephalopod-Inspired Design of Electro-Mechano-Chemically Responsive Elastomers for On-Demand Fluorescent Patterning. Nat. Commun. 2014, 5, 4899.
11. Kim, Y.J.; Wu, W.; Chun, S.E.; Whitacre, J.F.; Bettinger C.J. Biologically Derived Melanin Electrodes in Aqueous Sodium-ion Energy Storage Devices. *Proc. Natl. Acad. Sci. U.S.A.,* **2013***, 110,* 20912–20917.
12. Ding, D.; Guerette, P.A.; Fu, J.; Zhang, L.; Irvine, S.A.; Miserez, A. From Soft Self-Healing Gels to Stiff Films in Suckerin-Based Materials Through Modulation of Crosslink Density and β-Sheet Content. *Adv. Mater.* **2015***, 27*, 3953–3961.
13. Guerette, P.A.; Hoon, S.; Ding, D.; Amini, S.; Masic, A.; Ravi, V.; Venkatesh, B.; Weaver, J.C.; Miserez, A. Nanoconfined β-Sheets Mechanically Reinforce the Supra-Biomolecular Network of Robust Squid Sucker Ring Teeth. *ACS Nano*. **2014**, *8,* 7170–7179.

14. Zhong, C.; Deng, Y.; Roudsari, A. F.; Kapetanovic, A.; M. P. Anantram, M. P.; Rolandi, M. A Polysaccharide Bioprotonic Field-Effect Transistor. *Nat. Commun.* **2011**, *2*, 476.

15. Deng, Y.; Josberger, E.; Jin, J.; Rousdari, A.F.; Helms, B. A.; Zhong, C.; M. P. Anantram, M.P.; Rolandi, M. H^+-type and OH^- -type Biological Protonic Semiconductors and Complementary Devices. *Sci. Rep.* **2013**, *3*, 2481.

16. Crookes, W. J.; Ding, L. L.; Huang, Q. L.; Kimbell, J. R.; Horwitz, J.; McFall-Ngai, M. J. Reflectins: The Unusual Proteins of Squid Reflective Tissues. *Science* **2004**, *303*, 235–238.

17. Kramer, R. M.; Crookes-Goodson, W. J.; Naik, R. R. The Self-Organizing Properties of Squid Reflectin Protein. Nat. Mater. 2007, 6, 533–538.

18. Tao, A. R.; DeMartini, D. G.; Izumi, M.; Sweeney, A. M.; Holt, A. L.; Morse, D. E. The Role of Protein in Assembly in Dynamically Tunable Bio-optical Tissues. *Biomaterials* **2010**, *31*, 793–801.

19. Izumi, M.; Sweeney, A. M.; Demartini, D. G.; Weaver, J. C.; Powers M. L.; Tao, A. R.; Silvas, T. V.; Kramer, R. M.; Crookes-Goodson, W. J.; Mäthger, L. M.; Naik, R. R.; Hanlon, R. T.; Morse, D. E. Changes in Reflectin Protein Phosphorylation Are Associated with Dynamic Iridescence in Squid. *J. R. Soc. Interface* **2010**, *7*, 549–560.

20. Qin, G.; Dennis, P. B.; Zhang, Y.; Hu, X.; Bressner, J. E.; Sun, Z.; Crookes-Goodson, W. J.; Naik, R. R.; Omenetto, F. G.; Kaplan, D. L. Recombinant Reflectin-based Optical Materials. *J. Polym. Sci., Part B: Polym. Phys.* **2013**, *51*, 254–264.

21. DeMartini, D.G.; Izumi, M.; Weaver, A. T.; Pandolofi, E.; Morse, D. E. Structures, Organization, and Function of Reflectin Proteins in Dynamically Tunable Reflective Cells. *J. Biol. Chem.* **2015**, *290*, 15238–15248.
22. Levenson, R.; Bracken, C.; Bush, N.; Morse, D.E. Cyclable Condensation and Hierarchical Assembly of Metastable Reflectin Proteins, the Drivers of Tunable Biophotonics. *J. Biol. Chem.* **2016**, *291*, 4058–4068.
23. Phan, L.; Walkup, W.G., IV; Ordinario, D. D.; Karshalev, E.; Jocson, J.-M.; Burke, A. M.; Gorodetsky, A. A. Reconfigurable Infrared Camouflage Coatings From a Cephalopod Protein. *Adv. Mater.* **2013**, *25*, 5621–5625.
24. Phan L.; Ordinario, D. D.; Karshalev, E.; Walkup, W. G., IV; Shenk, M.; Gorodetksy, A. A. Infrared Invisibility Stickers Inspired by Cephalopods. *J. Mater. Chem. C.* **2015**, *3*, 6493–6498.
25. Ordinario, D. D.; Phan, L.; Walkup, W. G., IV; Karshalev, E.; Jocson, J.-M.; Hüsken, N.; Gorodetsky, A. A. Bulk Protonic Conductivity in a Cephalopod Structural Protein. *Nat. Chem.* **2014**, *6*, 596–602.
26. Ordinario, D.; Phan, L.; Jocson, J.-M.; Nguyen, T.; Gorodetsky, A.A. Protonic Transistors from Thin Reflectin Films. *APL Mat.* **2015**, *3*, 014907.
27. Phan, L.; Kautz, R.; J. Arulmoli, J.; Kim, I. H.; Le, D. T. T.; Shenk, M. A.; Pathak, M. M.; Flanagan, L. A.; Tombola, F.; Gorodetsky, A. A. Reflectin as a Material for Neural Stem Cell Growth. *ACS Appl. Mater. Interfaces,* **2016**, *8*, 278–284.

28. Zhang, Z.; Smith. D. L. Determination of Amide Hydrogen Exchange by Mass Spectrometry: A New Tool for Protein Structure Elucidation. *Prot. Sci.* **1993**, *2*, 522–553.
29. Tsutsui, Y.; Wintrode, P. L. Hydrogen/Deuterium Exchange-Mass Spectrometry: A Powerful Tool for Probing Protein Structure, Dynamics and Interactions. **2007**, *14*, 2344–2358.
30. Marcsisin, S. R.; Engen, J.R. Hydrogen Exchange Mass Spectrometry: What is it and What Can it Tell Us? *Anal. Bioanal. Chem.* **2010**, *397*, 967–972.
31. Konerman, L.; Pan, J.; Liu, Y.-H.; Hydrogen Exchange Mass Spectroscopy for Studying Protein Structure and Dynamics. *Chem. Soc. Rev.* **2011**, *40*, 1224–1234.
32. Brudler, R.; Gessner, C. R.; Li, S.; Tyndall, S.; Getzoff, E. D.; Woods, V. L., Jr. PAS Domain Allostery and Light-induced Conformational Changes in Photoactive Yellow Protein upon I2 Intermediate Formation, Probed with Enhanced Hydrogen/Deuterium Exchange Mass Spectrometry. *J. Mol. Biol.* **2006,** *363*, 148–160.
33. Svergun, D. I.; Koch, M. H. J. Small-angle Scattering Studies of Biological Macromolecules in Solution. *Rep. Prog. Phys.* **2003**, *66*, 1735–1782.
34. Putnam, C.D.; Hammel, M.; Hura, G.L.; Tainer, J.A. X-ray Solution Scattering (SAXS) Combined with Crystallography and Computation: Defining Accurate Macromolecular Structures, Conformations and Assemblies in Solution *Q. Rev. Biophys.* **2007**, *40*, 191–285.

35. Hura, G. L.; Menon, A. L.; Hammel, M.; Rambo, R. P.; Poole F. L., II ; Tsutakawa, S. E.; Jenny, F. R., Jr.; Classen, S.; Frankel, K. A.; Hopkin, R.C.; Yang, S.; Scott, J. W.; Dillard, B. E.; Adams, M. W. W.; Tainer, J. A. Robust, High-throughput Solution Structural Analyses by Small Angle X-ray Scattering (SAXS). *Nat. Methods*, **2009**, *6*, 606–612.

36. Jacques, D. A.; Trewhella, J. Small-angle Scattering for Structural Biology - Expanding the Frontier While Avoiding the Pitfalls. *Protein Sci.* **2010**, *19*, 642–657.

37. Blanchet, C. E.; Svergun, D. I. Small-Angle X-Ray Scattering on Biological Macromolecules and Nanocomposites in Solution. *Ann. Rev. Phys. Chem.* **2013,** *64*, 37–54.

38. Skou, S.; Gillilan, R. E.; Ando, N. Synchrotron-based Small-angle X-ray Scattering of Proteins in Solution. *Nat. Protoc.* **2014**, *9*, 1727–1739.

39. Goldstein, J.; Newbury, D. E.; Echlin, P.; Joy, D. C.; Romig Jr., A. D.; Lyman, C. E.; Fiori, C.; Lifshin, E. *Scanning Electron Microscopy and X-Ray Microanalysis: A Text for Biologists, Materials Scientists, and Geologists*; Plenum: New York, 1981.

40. McMullan, D. Scanning Electron Microscopy 1928–1965. *Scanning* **1995**, *17*, 175–185.

41. Allen, T.D. Introduction to Electron Microscopy for Biologists, Methods in *Cell Biology*; Academic Press; Burlington, 2008.

42. Schatten, H. Scanning Electron Microscopy for the Life Sciences, Advances in *Microscopy and Microanalysis;* Cambridge University Press, Cambridge: UK, 2013.
43. Renaud, G.; Lazzari, R.; Leroy, F. Probing Surface and Interface Morphology with Grazing Incidence Small Angle X-Ray Scattering. *Surf. Sci. Rep.* **2009**, *64*, 255–380.
44. Rivnay, J.; Mannsfeld, S. C. B.; Miller, C. E.; Salleo, A.; Toney, M. F. Quantitative Determination of Organic Semiconductor Microstructure from the Molecular to Device Scale. *Chem. Rev.* **2012**, *112*, 5488–5519.
45. Müller-Buschbaum, P. The Active Layer Morphology of Organic Solar Cells Probed with Grazing Incidence Scattering Techniques. *Adv. Mater.* **2014**, *26*, 7692–7709.
46. Hexemer; A.; Müller-Buschbaum; P. Advanced Grazing-incidence Techniques for Modern Soft-matter Materials Analysis. *IUCrJ* , **2014**, *2,* 106–125.
47. Peterson, V. K.; Papadakis, C. M. Functional Materials Analysis Using *in situ* and *in operando* in X-ray and Neutron Scattering. *IUCrJ.* **2015**, *2*, 292–304.
48. Smilgies, D.-M. GISAXS and GIWAXS. http://staff.chess.cornell.edu/~smilgies/gisaxs/GISAXS.php (accessed December 2, 2015)
49. King, S; Washington, C.; Heenan, R. Polyoxyalkylene Block-copolymers Adsorbed In Hydrocarbon and Fluorocarbon Oil-in-water Emulsions. *Phys. Chem. Chem. Phys.* **2005**, *7*, 143–149.

50. Nobbmann, U.; A. Morfesis, A. Light Scattering and Nanoparticls. *Mater. Today* **2009**, *12*, 52–54.

51. *Dynamic Light Scattering (DLS)*, in ISO22412:2015, International Organization for Standardization, Geneva, Switzerland, 2015.

52. Nobbmann, U. Polydispersity—what does it mean for DLS and chromatography?, http://www.materials-talks.com/blog/2014/10/23/polydispersity-what-does-it-mean-for-dls-and-chromatography, (accessed: April 2016).

53. Pique, M. E.; Ten Eyck, L. F.; Roberts, V. A. Unpublished Results.

54. Konarev, P.V.; Volkov, V. V.; Sokolova, A.V.; Koch, M.H.J.; Svergun, D.I. PRIMUS - a Windows-PC based System for Small-angle Scattering Data Analysis. *J. Appl. Cryst.* **2003**, *36*, 1277–1282.

55. Ilavsky, J; Jemian, P. R. *Irena*: Tool Suite for Modeling and Analysis of Small-angle Scattering. *J. Appl. Crystallogr*. **2009**, *42*, 347–353.

56. Kline, S. R. Reduction and Analysis of SANS and USANS Data Using IGOR Pro. *J. Appl. Crystallogr..* **2006**, *39*, 895–900.

57. Beaucage, G. Approximations Leading to a Unified Exponential/Power-law Approach to Small-angle Scattering. *J. Appl. Crystallogr.* **1995**, *28*, 717–728.

58. Beaucage, G. Small-angle Scattering from Polymeric Mass Fractals of Arbitrary Mass-Fractal Dimension. *J. Appl. Crystallogr.* **1996**, *29*, 134.

59. Hammouda, B. Analysis of the Beaucage Model. *J. Appl. Crystallogr.* **2010**, *43*, 1474–1478.

60. Beaucage, G. Combined Small-Angle Scattering for Characterization of Hierarchically Structured Polymer Systems over Nano-to-Micron Meter: Part II Theory. In *Polymer Science: A Comprehensive Reference*; Matyjaszewski, K.; Möller, M., Eds.; Elsevier: Oxford, 2012; Vol.2, pp 399–409.
61. Robertus, C.; Philipse, W. H.; Joosten, J. G. H.; Levine, Y. K. Solution of the Percus-Yevick Approximation of the Multicomponent Adhesive Sphere System to the Small Angle X-ray Scattering from Microemulsions. *J. Chem. Phys.* **1989**, *90*, 4482–4490.
62. de Kruif, C. G.; Rouw, P. W.; Briels, W. J.; Duits, M. H. G.; Vrij, A.; May, R. P. Adhesive Hard-sphere Colloidal Dispersions. A Small-angle Neutron-scattering Study of Stickiness and the Structure Factor. *Langmuir* **1989**, *5*, 422–428.
63. de Kruif, C. G. Supra-aggregates of Casein Micelles as a Prelude to Coagulation. *J. Dairy Sci.* **1998**, *81*, 3019–3028.
64. Tuiner, R.; de Kruif, C. G. Stability of Casein Micelles in Milk. *J. Chem. Phys.* **2002**, *117*, 1290–1295.
65. Dalgleish, D. G.; Corredig, M.; The Structure of the Casein Micelle of Milk and Its Changes During Processing. *Ann. Rev. Food Sci. Technol.* **2012**, *3*, 449–467.
66. Burchard, W. Solution Properties of Branched Macromolecules Advances. In *Advances in Polymer Science*; Roovers, J., Ed.; Springer: Berlin, 1999; Vol.143, pp 113-194.

67. Striegel, A.; Yau, W. W.; Kirkland, J.J.; Bly, D.D. Modern Size-Exclusion Liquid Chromatography: Practice of Gel Permeation and Gel Filtration Chromatography, 2nd ed; Wiley: New York , 2009.

68. Guinier, A.; Fournet, G. In *Small-Angle Scattering of X-Rays*; Mayer, M.G., Ed.; Wiley: New York, 1955.

69. Kratky, O. Natural High Polymers in the Dissolved and Solid State, In *Small Angle X-Ray Scattering*; Glatter, O.; Kratky, O. Eds.; Academic Press: London, 1982; pp 361–386.

70. Glatter, O. A New Method for the Evaluation of Small-Angle X-ray Scattering Data *J. Appl. Crystallogr*. **1977**, *10*, 415–421.

71. M. Hammel, M; Fierobe, H.-P.; Czjzek, M.; Kurkal, V.; Smith, J. C.; Bayer, E. A.; Finet, S.; Receveur-Bréchot, V.; Structural Basis of Cellusome Efficiency Explored by Small Angle X-ray Scattering. *J. Biol. Chem.* **2005**, *280*, 38562–38568.

72. Glatter, O. The Interpretation of Real-Space Information from Small-Angle Scattering Experiments *J. Appl. Crystallogr*. **1979**, *12*, 166–175.

73. Schindelin, J.; Arganda-Carreras, I.; Frise, E.; Kaynig, V.; Longair, M.; Pietzsch, T.; Preibisch, S.; Rueden, C.; Saalfeld, S.; Schmid, B.; Tinevez, J. Y.; White, D. J.; Hartenstein, V.; Eliceiri, K.; Tomancak, P.; Cardona, A. Fiji: An Open-Source Platform for Biological−Image Analysis. *Nat. Methods* **2012**, *9*, 676–682.

74. Amenitsch, H.; Bernstorff, S.; Laggner, P. High-Flux Beamline for Small-Angle X-Ray Scattering at Elettra. *Rev. Sci. Instrum.* **1995**, *66*, 1624–1626.

75. Ilavsky, J., NIKA: Software for Two-dimensional Data Reduction. *J. Appl. Crystallogr.* **2012**, *45*, 324–328.
76. Müller-Buschbaum, P.; Gebhardt, R.; Roth, S. V.; Metwalli, E.; Doster, W. Effect of Calcium Concentration on the Structure of Casein Micelles in Thin Films. *Biophys. J.* **2007**, *93*, 960–968.
77. Gebhardt, R.; Burghammer, M.; Reikel, C.; Roth, S. V.; Müller-Buschbaum, P. Structural Changes of Casein Micelles in a Calcium Gradient Film. *Macromol. Biosci.* **2008**, *8*, 347–354.
78. Gebhardt, R.; Kulozik, U. Simulation of the Shape and Size of Casein Micelles in a Film State. *Food Funct.* **2014**, *5*, 780–785.
79. Kreplak, L.; Doucet, J; Dumas, P.; Briki, F. New Aspects of the Alpha-helix to Beta-sheet Transition in Stretched Hard Alpha-keratin Fibers. *Biophys. J.* **2004**, *87*, 640–647.
80. Martel, A.; Burghammer, M.; Davies, R.J.; Emanuela, C. D.; Vendrely, C.; Riekel, C. Silk Fiber Assembly Studied by Synchrotron Radiation SAXS/WAXS and Raman Spectroscopy. *J. Am. Chem. Soc.* **2008**, *130*, 17070–17074.
81. Elshemey, W.M.; Elfiky, A.A.; Gawad, W.A. Correlation to Protein Conformation of Wide-angle X-ray Scatter Parameters. *Protein J*, **2010**, *29*, 545–550.
82. Makowski, L. Characterization of Proteins with Wide-angle X-ray Solution Scattering (WAXS). *J. Struct. Funct. Genomics* **2010**, *11*, 9–19.

83. Mauritz, K. A.; Moore, R. B. State of Understanding of Nafion. *Chem. Rev.* **2004**, *104*, 4535–4385.
84. DeMartini, D. G.; Ghoshal, A.; Pandolfi, E.; Weaver, A. T.; Baum, M.; Morse, D. E. Dynamic Biophotonics: Female Squid Exhibit Sexually Dimorphic Tunable Leucophores and Iridocytes. J. Exp. Biol. 2013, 216, 3733–3741.
85. Mäthger, L. M.; Senft, S. L.; Gao, M.; Karaveli, S.; Bell, G. R. R.; Zia, R.; Kuzirian, A. M.; Dennis, P. B.; Crookes-Goodson, W. J.; Naik, R. R.; Kattawar, G. W.; Hanlon, R. T. Bright White Scattering from Protein Spheres in Color Changing, Flexible Cuttlefish Skin. Adv. Funct. Mater. 2013, 23, 3980–3989.
86. DeMartini, D. G.; Krogstad, D. V.; Morse, D. E. Membrane Invaginations Facilitate Reversible Water Flux Driving Tunable Iridescence in a Dynamic Biophotonic System. Proc. Natl. Acad. Sci. USA 2013, 110, 2552–2556.
87. Deravi, L. F.; Magyar, A. P.; Sheehy, S. P.; Bell, G. R. R.; Mäthger, L. M.; Senft, S. L.; Wardill, T. J.; Lane, W. S.; Kuzirian, A. M.; Hanlon, R. T.; Hu, E. L.; Parker, K. K. The Structure-Function Relationships of a Natural Nanoscale Photonic Device in Cuttlefish Chromatophores. J. R. Soc. Interface 2014, 11, 20130942.
88. Messenger, J. B. Cephalopod Chromatophores: Neurobiology and Natural History. Biol. Rev. 2001, 76, 473–528.

CHAPTER 3 Summary and Future Work

3.1 Summary

In summary, we reviewed the remarkable camouflage abilities of cephalopods (squid, octopus, and cuttlefish) and highlighted recently developed dynamic materials inspired by the color- and shape-changing adaptations of cephalopods. Moreover, we performed biophysical characterization of reflectin isoform A1 (RfA1) via scanning electron microscopy (SEM), small-angle x-ray scattering (SAXS), grazing incidence small-angle x-ray scattering (GISAXS), and grazing incidence wide-angle x-ray scattering (GIWAXS). Based on our comprehensive study, we infer that reflectin self-assembles into prolate nanoparticles in solution (dionized water) and subsequently into oblate nanoparticles in the solid-phase. The findings detailed above may hold implications for not only better understanding the mechanisms that cephalopods employ to dynamically control their coloration but also for the development of bioinspired proton conducting materials, modular infrared camouflage materials, and improved protein-based bioelectronic devices.

3.2 Future Work

In conclusion, our work summarizes current efforts towards developing dynamic materials which resembles the remarkable properties of those native to cephalopods and details our effort to understand the hierarchical self-assembly of reflectin A1 (RfA1) protein. The full-length, native RfA1 protein, however, has resisted atomic-level characterization, due in part to the protein’s inherent lack of specific secondary structure and in part due to the proteins large size, which makes identifying biophysical motifs on the single amino-acid level extraordinarily difficult.

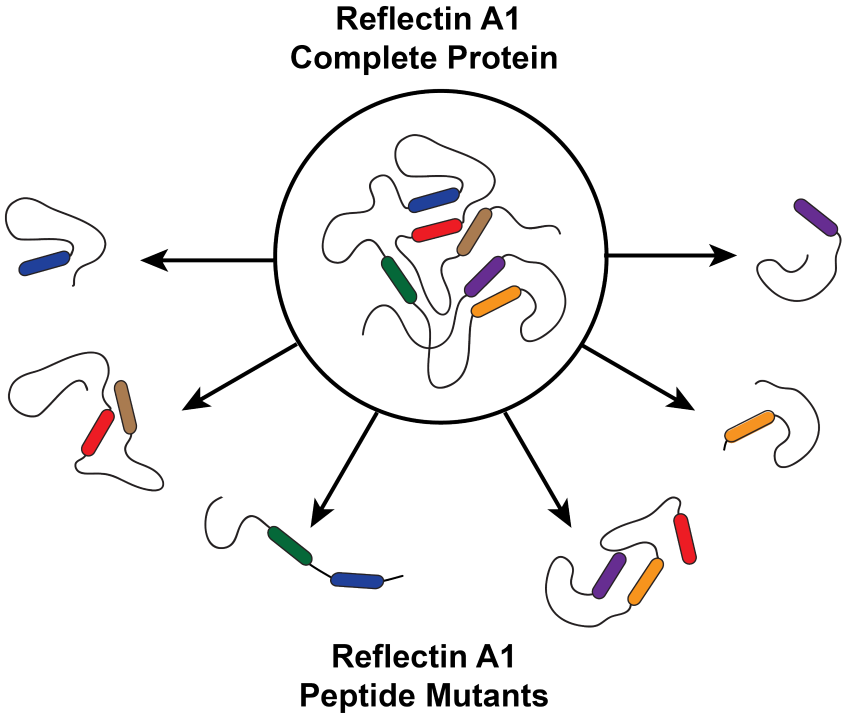

Figure 3.1 An illustration of a proposed approach to studying the reflectin family and synthesizing reflectin variants thereof. The RfA1 protein is composed of six similar amino acid sequences, which may be synthesized, characterized, and recombined into reflectin peptide mutants.

By studying a smaller, representative sequence, however, a more detailed, perhaps atomistic, understanding may be obtained by leveraging a SAXS and nuclear magnetic resonance (NMR). For example, a smaller (~8 kDa), representative RfA1 truncation mutant that consists of a single linker region and motif and possesses the same properties as the full length sequence.[1] The smaller, reflectin-like peptide makes a combined SAXS and NMR study possible from which atomic resolution detail can be gained. NMR signals from proteins can exhibit spectroscopic signals similar to small molecules, making resonance assignment possible for even disordered regions and large peptides, which in turn reveals both short and long-range structural details with atomic resolution.[2] SAXS, on the other hand, provides complementary information about the overall size and shape of the solution-phase protein.[3] This SAXS/ NMR approach in concert with physically motivated computational models would furnish structural information about reflectin that is not possible with x-ray crystallographic approaches alone and provides insight into the flexibility and function of these reflectin proteins both in advanced technologies and *in vivo*. We expect that our research will lead to an improved understanding of the reflectin protein family and of the multi-scale functionality of soft-matter in general.

3.3 References

1. Qin, G.; Dennis, P. B.; Zhang, Y.; Hu, X.; Bressner, J. E.; Sun, Z.; Crookes-Goodson, W. J.; Naik, R. R.; Omenetto, F. G.; Kaplan, D. L. Recombinant Reflectin-based Optical Materials. *J. Polym. Sci., Part B: Polym. Phys.* **2013**, *51*, 254–264.
2. Jenson, M. R., Zweckstetter, M., Huang, J., Blackledge, M., Exploring Free Energy Landscapes of Intrinsically Disordered Proteins at Atomic Resolution using NMR spectroscopy *Chem. Rev.* **2014**, *104*, 3607–3622.
3. Jacques, D. A.; Trewhella, J. Small-angle Scattering for Structural Biology - Expanding the Frontier While Avoiding the Pitfalls. *Protein Sci.* **2010**, *19*, 642–657.